The Meteoritical Society

Meteoritics & Planetary Science 57, Nr 3, 657–682 (2022)
doi: 10.1111/maps.13786

Sierra Gorda 013: Unusual CBa-like chondrite

Marina A. IVANOVA[1]*, Cyril A. LORENZ[1], Munir HUMAYUN[2], Shuying YANG[2], Chi MA[3], Svetlana N. TEPLYAKOVA[1], Ian A. FRANCHI[4], and Alexander V. KOROCHANTSEV[1]

[1]Vernadsky Institute of Geochemistry and Analytical Chemistry, Moscow 119991, Russia
[2]National High Magnetic Field Laboratory and Department of Earth, Ocean & Atmospheric Science, Florida State University, Tallahassee, 1800 E. Paul Dirac Drive, Tallahassee, Florida 32310, USA
[3]Division of Geological and Planetary Sciences, California Institute of Technology, Pasadena, California 91125, USA
[4]Planetary and Space Sciences Research Institute, Open University, Milton Keynes, MK7 6AA, UK
*Corresponding author. E-mail: meteorite2000@mail.ru

(Received 26 March 2021; revision accepted 22 December 2021)

Abstract–The new metal-enriched anomalous chondrite Sierra Gorda 013 (SG 013) contains two different lithologies. Lithology 1 (L1) is represented by anomalous CBa-like chondrite material containing ~80 vol% of Fe,Ni-metal particles and globules up to 6 mm in size; chondrules and clasts of types POP, BO, and SO (up to 5 mm in diameter); rare sulfides; and shock melted silicate–metal areas. It does not contain any fine-grained matrix. Several chondrules contain chromite–pyroxene symplectites. Lithology 2 (L2) has a recrystallized texture with evenly distributed olivine, pyroxene and plagioclase. L2 does not have any chondrules or sulfides, and contains less Fe,Ni- metal (~25 vol%) than L1. Both lithologies contain reduced olivine (Fa2–4) and pyroxene (Fs3.5), similar to CBa chondrites. Similar to CBa, there is no Ni-Co correlation in the SG 013 metal. Rare sulfides in L1 are enriched in V. Chromite was observed in both lithologies. Oxygen isotope compositions of both lithologies are different but in the range of CBa chondrites. Bulk major and trace element geochemistry of nonporphyritic chondrules and bulk siderophile compositions in metal globules of L1 indicate elemental fractionation during formation of metallic and silicate objects with records of the evaporation process: depletion in moderate and volatile elements with the exception of Cr. Bulk geochemistry of porphyritic chondrules of L1 and the silicate portion of L2 is similar and also indicates evaporation processes. The rare Earth element (REE) distribution of L1 chondrules records a very fractionated signature corresponding to possible differentiated precursor material, while the REE pattern of L2 is primitive chondritic. The formation of SG 013 could be explained by collisions of planetesimals producing an impact plume, the precursor material of which could be chondritic and possibly differentiated. Both lithologies were affected by secondary processes: L1 preserved the traces of shock events and partial melting resulting in formation of symplectites in chondrules, melt pockets, and metal–silicate melt between the metal globules; L2 was affected by shock thermal metamorphism (up to 900 °C) resulting in recrystallization.

INTRODUCTION

The CH and CB chondrites are meteorites enriched in metal: CH and CB chondrites contain >20 vol% and >60 vol% of metal, respectively (Krot et al., 2002; Weisberg et al., 1995). Weisberg et al. (1995) assigned the CH and CB chondrites to the CR chondrite clan. However, the CR clan meteorites could not have formed at the same time since many chondrules in CR chondrites have ancient U-Pb ages (Amelin & Krot, 2002) and show the presence of ^{26}Mg*. CB chondrites (Olsen et al., 2013) formed during a single-stage late event after nearly complete decay of ^{26}Al (Krot et al., 2018).

CH and CB chondrites have similar characteristics: high metal abundance compared to other known

chondrites, extreme depletion in moderately volatile elements, extreme enrichment in bulk $\delta^{15}N$, similar bulk oxygen isotopic compositions, high abundance of nonporphyritic chondrules, and absence of fine-grained matrix material between chondrules (Krot et al., 2002, 2014; Wasson & Kallemeyn, 1990; Weisberg et al., 1990, 1995).

Currently, one CB chondrite fall (Gujba) and 20 finds are known, including several paired Antarctic finds. The CB chondrites are divided into two subgroups based on their petrologic characteristics (Weisberg et al., 2001): coarse-grained CBa (e.g., Bencubbin, Weatherford, Gujba, Miller Range 05802) and a recently described chondrite, Quebrada Chimborazo (QC) 001 (Koch et al., 2016, 2019), and the fine-grained CBb (e.g., Hammadah al Hamra [HH] 237 and Queen Alexandra Range [QUE] 94411/94627; e.g., Krot et al., 2002). The CBa chondrites are characterized by very high metal abundances (40–80 vol%; e.g., Campbell et al., 2002; Kallemeyn et al., 1978; Newsom & Drake, 1979; Rubin et al., 2001; Weisberg & Ebel, 2009; Weisberg et al., 1990, 1995, 2001). They consist of large barred olivine (BO) and cryptocrystalline (CC) chondrules, both of centimeter-sized, angular to rounded fragments. Between these clasts, silicate–metal melt material occurs and is probably a product of shock metamorphism (Meibom et al., 2005). CBa chondrites contain high-pressure mineral phases (Koch et al., 2019; Weisberg et al., 2001). Fe,Ni-metal is unzoned in CBa chondrites.

The CBb chondrites (Krot et al., 2002; Weisberg et al., 2001) contain up to 80 vol% of metal, and the metal grains are mostly chemically zoned Fe,Ni-metal. CC chondrules are predominant and nonporphyritic (skeletal olivine [SO]) magnesian chondrules are less abundant. The chondrules have a narrow range of oxygen isotope compositions ($\Delta^{17}O \sim -2.5 \pm 0.5‰$; Krot et al., 2010). Small refractory inclusions are abundant, some are surrounded by high-temperature igneous rims, and they have more negative values of $\Delta^{17}O$ (from -15 to $-5‰$; Krot et al., 2017). The CBb chondrites contain rare hydrated lithic clasts, are similar in some respects to the CH chondrites, and may represent different samples of chondritic components formed by both nebular and shock processes (Campbell et al., 2005; Krot et al., 2008, 2010, 2012; Weisberg et al., 2001).

Several meteorites appear to have close relationships with CB chondrites. The Isheyevo meteorite (CH/CBb) has the characteristics of both CH and CBb chondrites (Ivanova et al., 2008) and contains up to 80 vol% in its metal-rich lithology. Another meteorite, Fountain Hills, is closely related to the CBa subtype (Lauretta et al., 2009; Weisberg & Ebel, 2009). However, many features of this meteorite are distinct from the other CB chondrites. It contains 26 vol% of Fe,Ni-metal, significantly lower than other CBa chondrites. In addition, Fountain Hills contains porphyritic chondrules, which are extremely rare in other CBa chondrites. Fountain Hills does not appear to have experienced the extensive shock seen in other CB chondrites. The data for Fountain Hills are consistent with formation in a highly energetic thermal event in a dusty region of the solar nebula (e.g., Campbell et al., 2001) or a giant impact plume (e.g., Krot et al., 2005). The new ungrouped chondrites Northwest Africa (NWA) 12273 and 12379 contain 60 vol% of metal, but have affinities to L/LL chondrites based on mineral chemistry and oxygen isotopic compositions (Agee et al., 2019; Jansen et al., 2019).

For many years, it has been proposed that CB chondrite chondrules and other components form in the early solar nebula (Campbell et al., 2001; Krot et al., 2002; Meibom et al., 1999; Newsom & Drake, 1979; Weisberg et al., 1990, 2001), but other arguments favor the hypothesis that CBs are products of protoplanetary collisions (e.g., Amelin & Krot, 2005; Campbell et al., 2002; Fedkin et al., 2015; Krot et al., 2005; Oulton et al., 2016; Wasson & Kallemeyn, 1990). Most chondrules in CBs and a significant portion of chondrules in CHs appear to have resulted from a collisional event between planetary bodies 4562.76 ± 0.5 Myr, ~4.5 Myr, after the formation of CV calcium-aluminum-rich inclusions (CAI s; 4567.26 ± 0.7 Myr ago, Connelly et al., 2012), with the canonical initial $^{26}Al/^{27}Al$ ratio of $(5.25 \pm 0.02) \times 10^{-5}$ (Bollard et al., 2015; Krot et al., 2005; Olsen et al., 2013), which are the oldest dated solids that originated in the solar system.

A new chondrite enriched in metal was found recently in Chile, Sierra Gorda (SG) 013. Here, we present the results of a study of this chondrite, which is unusual due to the presence of chondritic and achondritic lithologies (Gattacceca et al., 2020). We describe its petrography, mineral chemistry, trace element geochemistry of Fe,Ni-metal and silicate chondrules, and bulk oxygen isotopic composition. We also compare these characteristics with those of well-known members of CB chondrites and based on the history of the CB parent body(s) discussed above.

ANALYTICAL PROCEDURE AND SAMPLES

Two polished sections of total surface area (~6.25 cm^2) of Sierra Gorda 013 L1 and one polished section (~2.5 cm^2) of L2 were studied by optical microscopy at the Vernadsky Institute (Russia). Backscattered electron (BSE) imaging and energy-dispersive X-ray spectroscopy (EDS) analyses were performed using the Tescan scanning

electron microscope (SEM) with analytical equipment of the Oxford Instruments AztecLive Automate with detector UltimMax 100 (Tescan, Russia) and FEI Nova NanoSEM 600 SEM at the Smithsonian Institution (USA). FEI Nova NanoSEM 600 SEM is equipped with a Thermo Electron energy-dispersive X-ray spectrometer and Noran System Six software. The SEM was operated at 15 kV with a beam current of 2–3 nA. Half of the section was subsequently mapped in Si, Mg, Fe, Ca, Al, Ti, Fe, Ni, S, Cr, P X-rays using the FEI Nova NanoSEM 600. For both instruments, the fully focused electron beams were operated at 15 kV accelerating voltage, 100 nA beam current, 20–30 ms per pixel acquisition time, and a spatial resolution of ~2–3 μm per pixel.

Mineral compositions were analyzed with a JEOL JXA-8530+ Hyperprobe five-spectrometer electron microprobe at the Smithsonian Institution. Operating conditions were 15 kV accelerating voltage, a fully focused beam with 20 nA beam current, and peak counting times of 20 s for major elements and 40 s for minor elements. Natural and synthetic minerals were used both as calibration standards and, in some cases, as unknowns that were analyzed at the beginning and the end of every run: San Carlos olivine for Mg, Fe, and Ni; wollastonite for Si and Ca; spinel for Al; diopside for Mg, Ca, and Si; anorthite for Al and Ca; albite for Na; orthoclase for K; hornblende for Ti and K; ilmenite for Ti; chromite for Cr; manganite for Mn. Matrix corrections were applied using Phi-Rho-Z (for JEOL JXA 8530+) software routines. Detection limits for silicates were (in wt%) SiO_2, TiO_2, Al_2O_3, Cr_2O_3, FeO, MnO, MgO, CaO, NiO—0.02; K_2O, Na_2O—0.05. Peak overlaps were taken into account.

For the metal and sulfide analyses, we used a focused beam with a current of 20 nA and an accelerating voltage of 15 kV. We quantified the abundances of Si, Fe, Cr, S, Mn, P, Ni, and Co. We used diopside as the Si standard, pure iron metal for Fe, pure chromium metal for Cr, troilite for S, schreibersite for P, pure nickel metal for Ni, pure cobalt metal for Co, pure manganese for Mn. Detection limits, in wt%, are as follows: 0.02 for Si, 0.02 for Fe, 0.05 for Cr, 0.03 for S, 0.05 for Mn, 0.02 for P, 0.03 for Ni, and 0.03 for Co.

The modal abundances were estimated based on high-resolution BSE images using Adobe Photoshop™ software. Electron backscatter diffraction (EBSD) analyses of a new sulfide phase were performed using an HKL EBSD system on the ZEISS 1550VP SEM at the California Institute of Technology (USA), operated at 20 kV and 6 nA in focused beam mode with a 70° tilted stage and variable pressure mode (25 Pa) using procedures described in Ma and Rossman (2008). The EBSD system was calibrated using a single-crystal silicon standard.

Laser Ablation ICP-MS Analysis of Elemental Abundances

Two sections of SG 013 (L1 and L2) were analyzed using an Elemental Scientific Lasers New Wave™ UP193FX excimer laser ablation system coupled to a Thermo Element XR™, inductively coupled plasma mass spectrometer (LA-ICP-MS) at the Plasma Analytical Facility, Florida State University. Analyzed points are represented in Figs. S1a and S1b in the supporting information. The oxide production was set by tuning the sample gas to yield ThO^+/Th^+ <1%. Metal and sulfide particles were measured with a 50 μm spot, at 50 Hz repetition rate, and 10 s of ablation per spot following Humayun et al. (2010) and Humayun (2012). Standards used were USGS silicate glasses GSC-1g, GSD-1g, and GSE-1g; NIST SRM 1263a steel; and the iron meteorites Hoba (IVB) and North Chile (Filomena, IIA). Silicate clasts were measured with either spot, line, or raster modes at 50 Hz repetition rate. Spots were taken with 100 μm spot size and 10 s of ablation per spot. Lines were taken with 50 μm spot size scanned at 10 μm s^{-1}. Rasters were taken with 100 μm spot size scanned at 20 or 25 μm s^{-1} covering areas of about 300 × 800 μm. Major and trace element concentrations for silicates were standardized with USGS silicate glasses GSC-1g, GSD-1g, BHVO-2g, BCR-2g, and BIR-1g (Yang et al., 2020).

Oxygen Isotope Compositions

Separate splits of L1 and L2, weighing ~50 mg each, were used to measure bulk oxygen isotope composition at the Open University (UK). The samples were crushed in an agate mortar and pestle. Oxygen isotope compositions were determined in replicate on ~2 mg aliquots of the partly homogenized sample by laser fluorination. The samples were heated with a CO_2 laser (10.6 nm) in the presence of excess BrF_5, the gas purified over hot KBr and cryogenic traps, and then analyzed on a PRISM III mass spectrometer (VG Isogas Ltd). Details of the procedure are described by Miller et al. (1999). Changes to analytical procedures implemented subsequent to the system description given by Miller et al. (1999) have resulted in improvements to precision such that 39 analyses of our internal obsidian standard undertaken during six separate sessions in 2013 gave the following combined results: ±0.052‰ for $\delta^{17}O$; ±0.093‰ for $\delta^{18}O$; ±0.017‰ for $\Delta^{17}O$ (2σ) (Greenwood et al., 2016).

RESULTS

SG 013 was found as several individual fragments 300 km apart from the QC 001 CBa chondrite according to the Meteoritical Bulletin Database (Bouvier et al., 2017). Based on the distance between their respective locations and considering their different textures and mineral compositions, these meteorites are not paired. SG 013 contains two lithologies (Fig. 1) and all separate samples of the meteorite were found in one small area. The main mass consists of lithology L1 (Figs. 1a and 1b) and is represented by two fragments recovered within 0.5 m of each other. Numerous meteorite fragments of lithology L2 (Fig. 1c) were located in an area of 1 m^2 around the place where the main mass samples were found. Stones containing both of the lithologies were not found.

Petrography

L1 (Figs. 1a and 1b) contains low-Ni Fe,Ni-metal (~80 vol%) represented by large globules up to 0.9 cm in size, and smaller metallic particles. The metal globules often contain inclusions of silicate clasts and inclusions embedded in metal at the metal–silicate boundaries (Fig. 1d). These inclusions mostly consist of pyroxene, but rarely of olivine and pyroxene, 5–50 μm in size. In some metal globules, tiny inclusions of glass (up to 20 μm) were also observed. Porphyritic pyroxene (PP) and olivine–pyroxene (POP) chondrules, BO and SO chondrules (Figs. 2a–c), up to 0.6 cm in size, in equal amount occur between the metal spherules; matrix is absent (Fig. 1a). Angular fragments of chondrules, termed clasts, predominate compared to round-shaped chondrules (Fig. 1a).

PP chondrules contain pyroxene embedded in mesostasis. POP chondrules consist of olivine, low-Ca pyroxene, Ca-pyroxene, and mesostasis (Fig. 2a). Often chondrules contain a massive olivine core surrounded by a pyroxene rim. BO chondrules (Fig. 2b) mostly consist of bars of olivine with mesostasis between bars. SO chondrules (Figs. 2c and 2d) contain skeletal olivine, Ca-pyroxene, and Ca-pyroxene embedded in glass (Fig. 2d). Mesostasis in all chondrules and clasts of L1 is represented by Ca-pyroxene and glass (Fig. 2e). A silicate–metal shock melt containing blebs of Fe,Ni-metal, silicate inclusions, and terrestrial iron hydroxides was observed around and between chondrules, angular silicate clasts, and Fe,Ni-metal (Fig. 2f).

Several BO chondrules and fragments contain symplectites of chromite and pyroxene (Figs. 2b and 3a). Some symplectite-bearing chondrules have the bars of olivine growing in alignment with the outer surface of the chondrule along the contact with the Fe,Ni-metal (Fig. 2b). Symplectites (up to 30 μm across) are intergrowths of chromite, clinopyroxene, and enstatite (Figs. 3a and 3b). Symplectites are located on the contacts of olivine or enstatite with the chondrule mesostasis and inside olivine or enstatite grains.

Minor minerals are daubreelite (Fig. 4a), brezinaite (Fig. 4b), schreibersite, and magnesiochromite. They occur as separated grains and inclusions in metal. An unknown V-rich sulfide (~1 μm in size) was found in daubreelite (Fig. 4c). In Fe,Ni-metal, one unusual assemblage of daubreelite with chromite was observed (Fig. 4d), and an assemblage of chromite with daubreelite enclosing a small grain of rutile was found in a contact of olivine and pyroxene (Fig. 4e). Many chondrules contain chromite grains. In SO chondrules and clasts, chromite is concentrated in the peripheral part consisting of low-Ca pyroxene embedded in mesostasis, compared to the central part, which consists of olivine, Ca-pyroxene, low-Ca-pyroxene, and mesostasis (Fig. 4f). Schreibersite occurs as separate grains and inclusions in Fe,Ni-metal or as intergrowth with Fe,Ni-metal and sulfides.

The shock stage of most chondrules from L1 is characterized by undulatory extinction of olivine corresponding to a low shock stage, S2 (Stoffler et al., 1991), but several fragments have stages S4–5 based on mosaic extinction of olivine grains and impact melt areas. Abundant melt pockets enclosing tiny blebs of Fe,Ni-metal occur mostly along the boundaries of chondrules and some angular silicate fragments (Fig. 2f).

L2 (Fig. 5a) is a crystalline rock, and it has a lower abundance of Fe,Ni-metal (~25%), which occurs as particles up to 1 mm in size, between evenly distributed coarse-grained silicates: ~75%, olivine, pyroxene, anorthite, chromite, and very rare schreibersite (Fig. 5b). Only one small grain of schreibersite was found in a contact of the metal particle. Unlike L1, L2 lacks sulfides. Crystals are mostly anhedral, sometimes round, olivine and low-Ca pyroxene are up to 150–200 μm, diopside and anorthite up to 50 μm, no chondrules were observed in L2 (Figs. 5a and 5b). This lithology contains many subparallel fractures filled by weathering products (Figs. 1c, 5a, and 5b), which cut all minerals and the metal grains. L2 is characterized by low shock features based on the weak undulatory extinction (almost sharp) of olivine (S2, Stoffler et al., 1991).

Mineral Chemistry

The chemical composition of olivine from both lithologies of SG 013 is very homogeneous and highly magnesian. In L1, olivine is Fa 2.70 ± 0.14 mole%

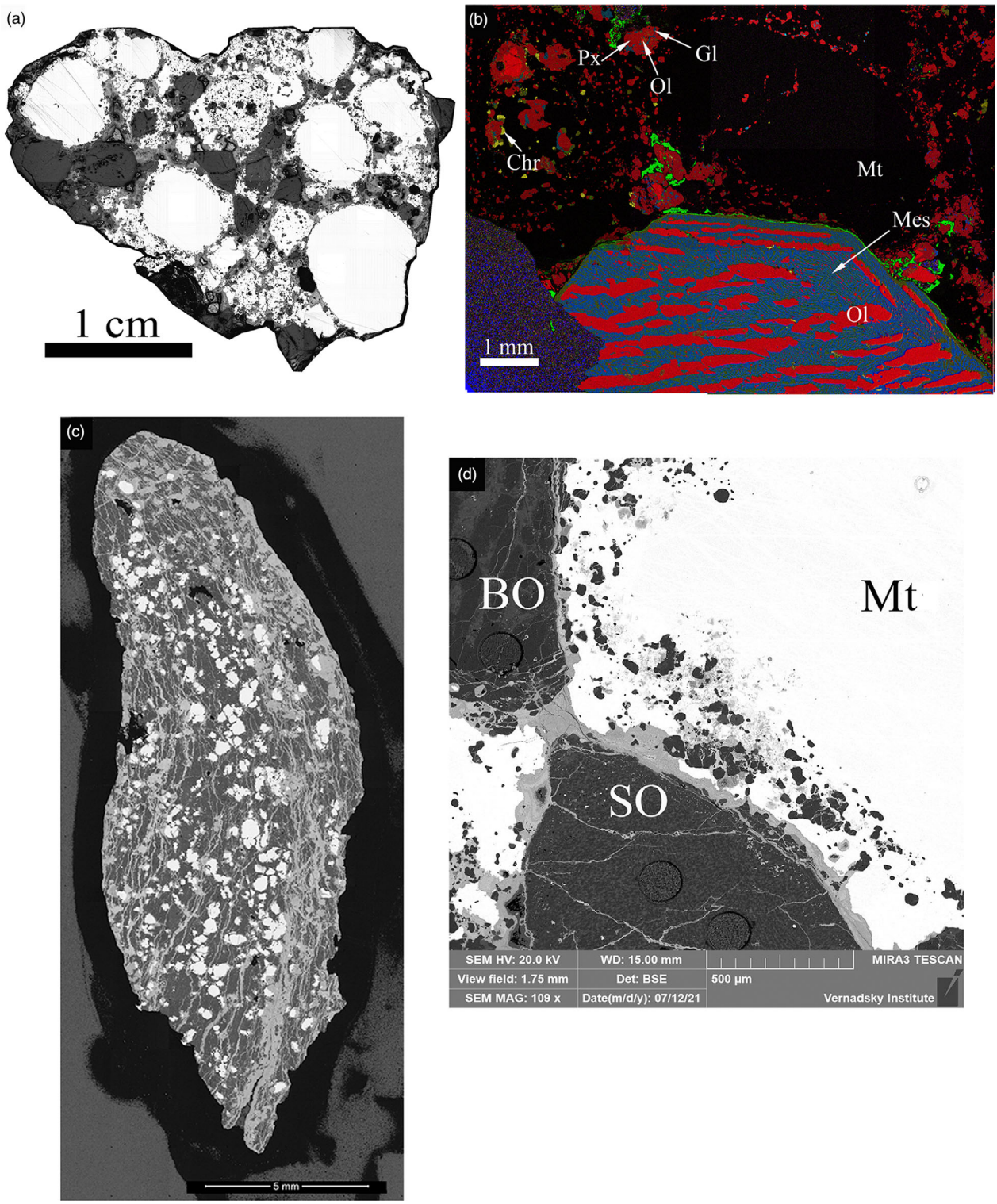

Fig. 1. Lithologies (L1) and (L2) from SG 013: (a) optical view (reflected light) of L1. It is typical CBa chondrite in texture and consists of Fe,Ni-metal globules (~80 vol%), up to 0.8 cm; BO and POP chondrules and their clasts up to 0.7 cm; matrix is absent; (b) X-ray elemental map in Kα (Mg—red, Ca—green, Al—blue, Cr—yellow, epoxy—purple) of a fragment of SG 013 material of L1 with a BO chondrule and metal containing silicate fragments; (c) backscattered electron image of L2 containing ~25 vol% of Fe,Ni-metal; (d) metal globule containing silicate fragments in periphery of the globule in contact with BO and SO clasts. Mt = Fe,Ni–metal; Chr = chromite; Px = pyroxene; Ol = olivine, Ca-Px = Ca-pyroxene, Gl = glass. (Color figure can be viewed at wileyonlinelibrary.com.)

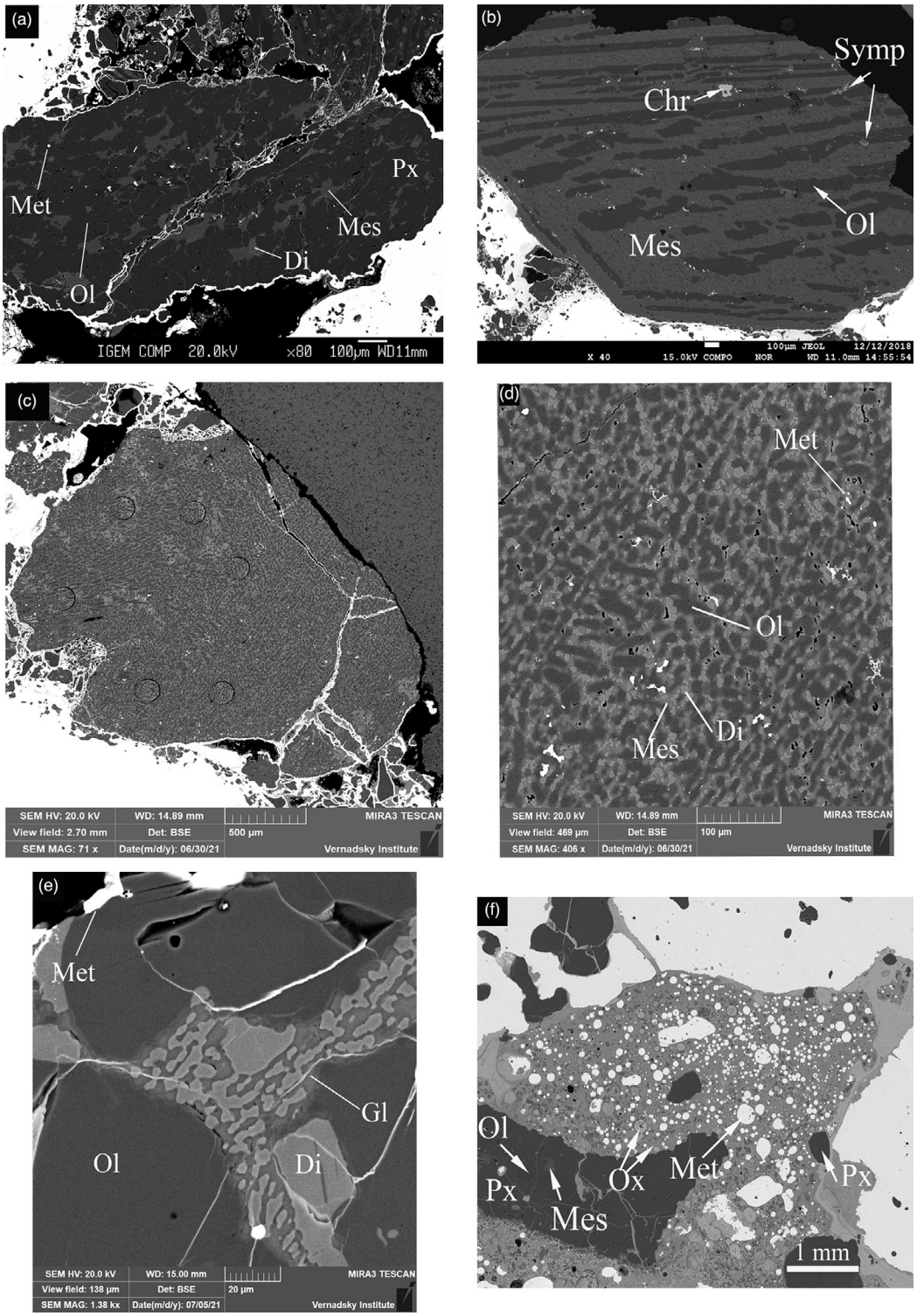

Fig. 2. Backscattered electron images of several constituents of lithology 1 from SG 013: (a) POP chondrule consisting of olivine and pyroxene surrounded by mesostasis; (b) BO chondrule with symplectites (details in Figs. 3a and 3b), the symplectite-bearing chondrule has the bars of olivine growing in alignment with the outer surface of the chondrule along the contact with the Fe,Ni-metal; (c) clasts of SO chondrule; (d) texture of SO clasts, large scale; (e) mesostasis of POP chondrule consisting of glass and Ca-pyroxene; (f) metal–silicate shock melt between chondrule clast and Fe,Ni-metal. Ol = olivine; Px = low-Ca-pyroxene; Gl = glass; Symp = symplectites; Met = Fe,Ni-metal; Tr = troilite; Chr = chromite; Di = diopside; Mes = mesostasis; Ox = oxidized Fe,Ni-metal; BO = barred olivine chondrule; SO = skeletal olivine chondrule.

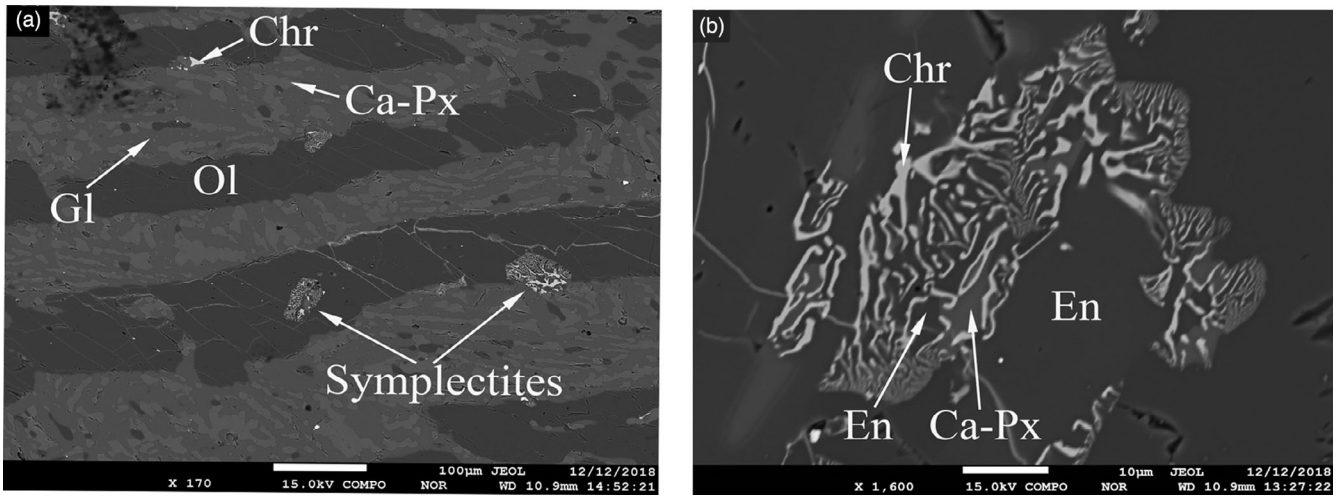

Fig. 3. Backscattered electron images of symplectite in lithology 1 of SG 013: (a) several symplectites in the BO chondrule; (b) symplectite consisting of chromite, enstatite, and Ca-pyroxene from the BO chondrule. En = enstatite; Chr = chromite; Ol = olivine; Gl = glass; Ca-Px = Ca-pyroxene.

(N = 29), Fe/Mn = 16.8 ± 1.5 atom%; in L2, olivine is Fa 2.10 ± 0.10 mole% (N = 53), Fe/Mn = 12.9 ± 1.5 atom% (Table 1). In both lithologies, the contents of CaO and Cr_2O_3 in olivine are very low (0.03 ± 0.01 and 0.25 ± 0.14 wt%, respectively) compared to olivine from Bencubbin, Weatherford (Weisberg et al., 2001), and Fountain Hills (Lauretta et al., 2009) (Figs. 6a and 6b), and MnO content is similar to Bencubbin (0.16 ± 0.01 wt%) (Fig. 6c), higher than in Fountain Hills and Weatherford.

Pyroxene in L1 and L2 is represented by low-Ca pyroxene and Ca-pyroxene, diopside. The low-Ca pyroxene is similar in both lithologies (Fs 3.53 ± 0.24, Wo 1.41 ± 0.20, Fe/Mn = 12.0 ± 1.9 atom%) (Table 1). Diopside in L1 (Fs 1.68 ± 0.09, Wo 45.4 ± 0.79, Fe/Mn = 8.87 ± 1.8 atom%) has lower Fs content than that in L2 (Fs 2.10 ± 0.51, Wo 45.8 ± 0.5, Fe/Mn = 10.8 ± 4.6 atom%) (Table 1). Pyroxenes, enstatite, and diopside in symplectites are enriched in Cr_2O_3 content up to 2.5 wt%, which may be a result of overlapping of the phases during EPMA analyses due to small grain sizes.

Chondrules from L1 have only anisotropic glass in the chondrule mesostasis (Table 1) and composition could be enriched in MgO (~1.1 wt%). Rare tiny glass inclusions in the metal globules are enriched in alkalis. Plagioclase from L2 is anorthite of very constant composition: An96.5 Ab3.36 (Table 1). Individual grains of chromite in both lithologies and symplectites in the chondrules from L1 have constant and similar chemical composition of magnesiochromite (Table 1) having an empirical formula of $(Mg_{0.81}Fe_{0\cdot19})(Cr_{1.38}Al_{0.62})O_4$. TiO_2 content in chromite is very low, 0.11 wt%.

Fe,Ni-metal in both lithologies is unzoned. Several representative analyses of Fi, Ni-metal from lithologies L1 and L2 are presented in Table 2. The low-Ni metal ("kamacite") in L1 and L2 contains on average 6.76 ± 0.37 wt% Ni, 0.39 ± 0.07 wt% Co. There is no Ni-Co correlation in the metal composition of SG 013 in both lithologies (Fig. 7) and the Co/Ni ratio (0.058) is almost solar (0.05; Anders & Grevesse, 1989). Chemical profiles across very rare small Fe,Ni-metal grains distinguish grains containing averages of 12.6 ± 0.2 and 24.1 ± 1.4 wt% Ni, 0.30 ± 0.02 and 0.18 ± 0.02 wt% Co (Fig. 7), and 0.05 ± 0.02 and 0.02 ± 0.01 wt% P, respectively. Schreibersite from L1 and L2 usually contains 15.4 wt% P and 35.9 wt% Ni (Table 2).

The sulfide assemblage in L1 is unusually enriched in V (Table 3) and represented by daubreelite $FeCr_2S_4$ (Fig. 4a), V-rich daubreelite ($Fe[Cr,V]_2S_4$) containing up to 2.0 wt% V, V-rich brezinaite $(Cr_{2.05}V_{0.62}Fe_{0.33})S$ (Fig. 4b) crystal structures of which were confirmed by the EBSD method. Unknown V,Fe,Cr-rich sulfide occurring as tiny mineral grains (<1 µm) in the V-rich daubreelite (Table 3; Fig. 4c) was investigated by EBSD, but we could not obtain reliable Kikuchi patterns of this mineral.

Geochemistry of Metal and Silicate Components

The locations of spots taken on metal and silicate objects from L1 analyzed by LA-ICP-MS are shown in Figs. S1a and S1b. Average chemical compositions of six large metal globules from L1 of SG 013 with standard deviations are presented in Table 4 and normalized to CI compositions are shown in Fig. 8. The metal globules show a wide range of siderophile element

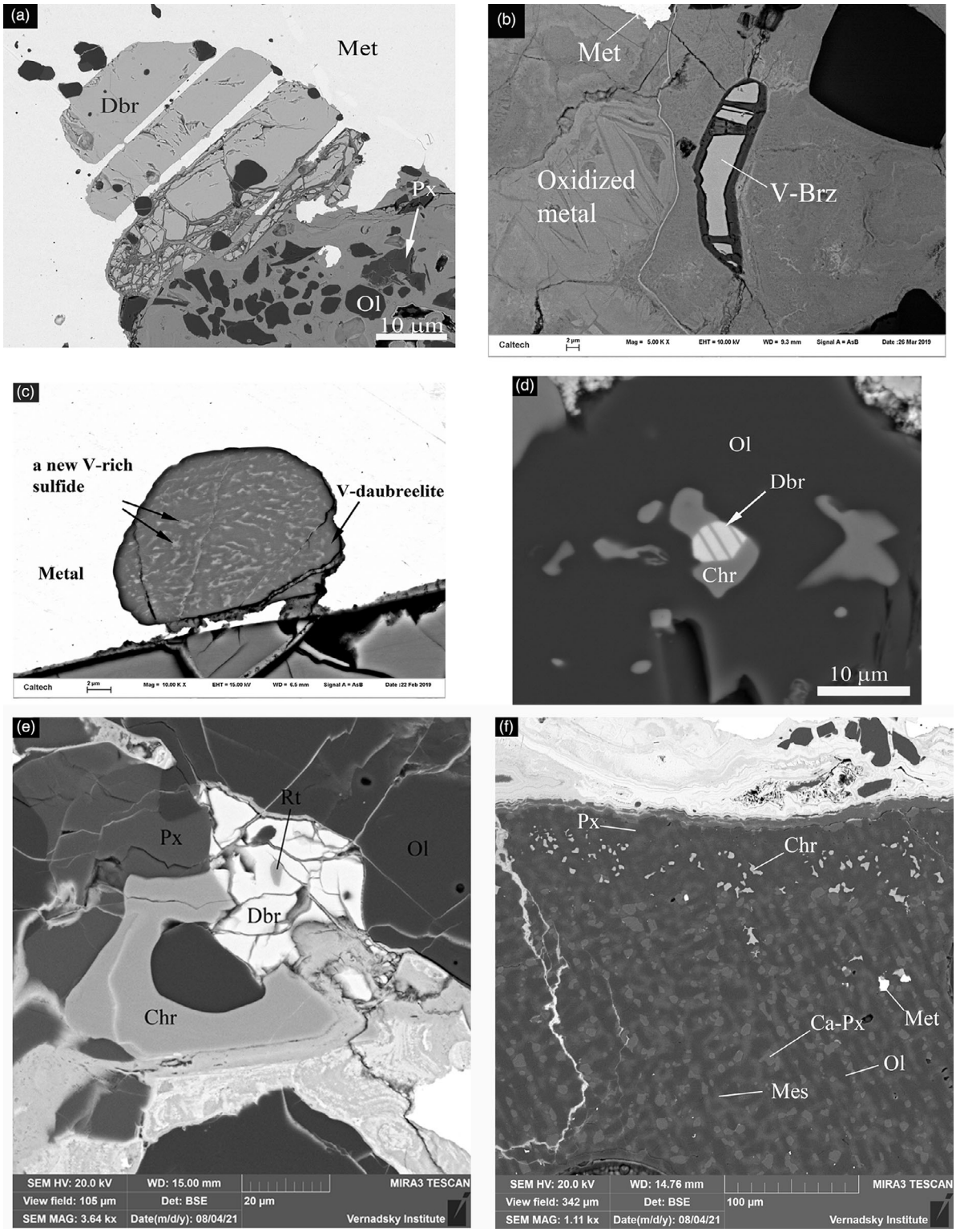

Fig. 4. Backscattered electron images of opaque minerals of lithology 1 from SG 013: (a) daubre elite grains in the metal; (b) V-brezinaite surrounded by oxidizing Fe,Ni-metal; (c) assemblage of a new V-rich sulfide and V-daubreelite in Fe,Ni-metal; (d) assemblage of daubreelite and chromite in olivine; (e) assemblage of rutile in daubreelite and chromite; (f) chromite in a periphery of a fragment of SO chondrule, a central part consists of olivine, Ca-pyroxene, and glassy mesostasis, a periphery of SO consists of low-Ca and Ca-pyroxene with small grains of chromite. Met = metal, Dbr = daubreelite, Chr = chromite, Rt = rutil, V-Brz = V-brezinaite; Ol = olivine, Px = low-Ca-pyroxene, Ca-Px = Ca-pyroxene.

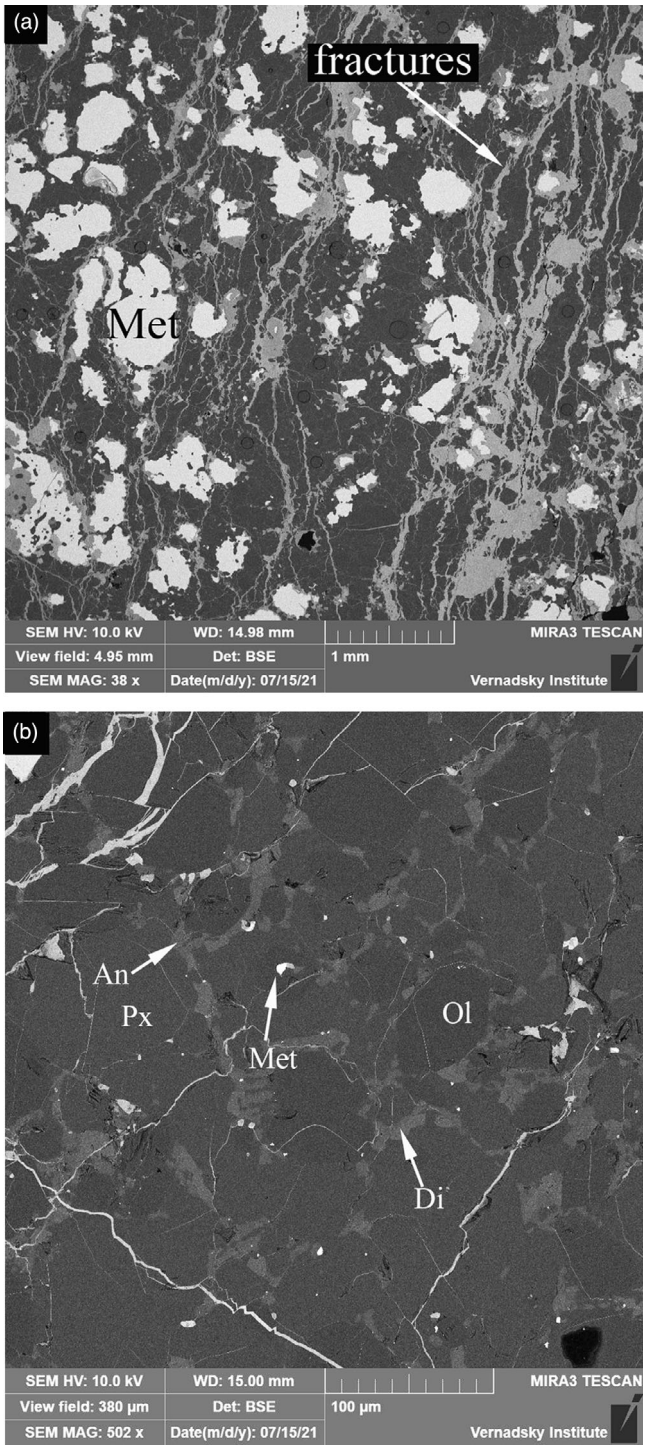

Fig. 5. Backscattered electron images of lithology 2 (L2): (a) recrystallized texture of L2 showing evenly distribution of Fe,Ni-metal and silicate grains in the rock; many fractures filled by iron hydroxides intersect the rock; (b) a fragment of L2 (large scale) showing olivine, low-Ca pyroxene, diopsides, and anorthite with recrystallized texture. An = anorthite; Ol = olivine; Px = low-Ca-pyroxene; Di = diopside; Met = metal.

compositions from more (spherule #6) to less (spherule #1) enriched in refractory elements in comparison to the chondritic metal, while the medium and highly volatile elements have similar abundances. The metal globules which are more enriched in refractory siderophiles are similar to those in the Bencubbin CBa chondrites (Campbell et al., 2002) (Fig. 8a).

Average chemical compositions with standard deviations of 11 silicate chondrules and clasts from L1 of SG 013 in oxides and elements obtained by LA-ICP-MS are presented in Table 5. All analyzed objects from L1 are represented in Fig. S2 and include 4 SO (#1, #2, #3, #11), 4 POP (#4, #8, #9, #10), 2 BO (#5, #6), and 1 PP (#7) chondrules and clasts. Bulk average compositions of POP, SO, BO chondrules and clasts normalized to CI composition are presented in Fig. 9a. Bulk rare Earth element (REE) compositions of each chondrule and clast are shown in Fig. 9b. Similar to the siderophile element patterns in metal, the silicate chondrules and clasts in L1 are very diverse, judging by major and some trace elements (Fig. 9a) and REE patterns (Fig. 9b). SO, BO, and PP chondrules are enriched in refractory lithophile elements (2–7 × CI) and in moderate volatile elements (1.5–5 × CI) from V to Mn with a minimum in Fe, and highly depleted in volatile elements beginning from Mn. POP chondrules are slightly enriched in refractory and moderate lithophile elements (1.2–2.7 × CI), but this enrichment is less than that in SO, BO, and PP chondrules with a minimum in Fe content (Fig. 9a). POP chondrules are depleted in volatile elements beginning from Mn similar to SO, BO, and PP chondrules.

Several chondrules of L1 are light REE (LREE) depleted (#4, #10), and others are LREE enriched with fractionated patterns (#1, #2, #3, #5, #6, #7). A plot of Gd/Yb versus La (all elements CI normalized) clearly shows that there is a correlation between LREE enrichment and the slope of the REE pattern in all the SG 013 silicate chondrules and clasts (Fig. 10). All the chondrules and clasts of L1 exhibit a weak positive Ce anomaly.

The locations of areas taken on silicates from L2 analyzed by LA-ICP-MS are shown in Fig. S1c. Chemical compositions of several silicate areas of L2 consisting of olivine, pyroxene, plagioclase, and rare chromite as well as bulk raster analyses with average and standard deviation are represented in oxides and elements in Table 5. Average compositions of silicate areas of L2 normalized to CI composition with standard deviations are shown in Fig. 9a. It is interesting to note that L2 demonstrates enrichment in refractory and moderate volatile elements similar to that of POP chondrules from L1 (Fig. 9a). REE

Table 1. Chemical composition of silicate minerals and chromite from lithologies (L1) and (L2) of SG 013 (wt%).

	No.	SiO_2	TiO_2	Al_2O_3	Cr_2O_3	FeO	MnO	MgO	CaO	Na_2O	K_2O	NiO	Total	Fs	Wo	An	Ab	Fa	Fe/Mn
Olivine (L1)	31	41.75	0.04	0.05	0.25	2.73	0.16	55.15	0.04	b.d.	b.d.	b.d.	100.2					2.70	16.80
	2σ	0.33	0.02	0.03	0.14	0.12	0.01	0.70	0.01									0.13	1.50
Olivine (L2)	52	41.60	b.d.	0.05	0.10	2.12	0.16	56.55	0.03	b.d.	b.d.	b.d.	100.6					2.10	12.90
	2σ	0.14		0.05	0.06	0.10	0.01	0.16	0.01									0.10	1.50
Low-Ca-pyroxene (L1)	33	57.90	0.19	1.02	0.92	2.26	0.19	37.04	0.77	b.d.	b.d.	0.04	100.3	3.53	1.41				12.21
	2σ	0.20	0.03	0.13	0.09	0.18	0.02	0.26	0.11	0.00	0.00	0.03		0.24	0.20				1.84
Low-Ca-pyroxene (L2)	46	57.48	0.21	0.94	0.87	2.02	0.19	37.41	1.03	b.d.	b.d.	b.d.	100.1	3.15	1.87				10.57
	2σ	0.14	0.03	0.12	0.09	0.13	0.01	0.17	0.09					0.18	0.17				1.29
Diopside (L1)	16	54.11	0.58	2.14	1.23	0.95	0.10	18.57	22.09	0.08	b.d.	b.d.	99.8	1.69	45.31				9.06
	2σ	0.60	0.09	0.39	0.15	0.07	0.02	0.25	0.44	0.01				0.10	0.76				1.97
Diopside (L2)	17	52.98	0.62	2.00	1.09	1.24	0.11	18.93	23.13	0.08	b.d.	0.05	100.3	2.10	45.78				10.81
	2σ	0.38	0.07	0.16	0.08	0.35	0.01	0.23	0.27	0.01		0.03		0.51	0.48				4.65
Glass in mesostasis (L1)	10	44.72	0.04	35.05	0.03	0.31	b.d.	0.64	17.81	0.42	b.d.	0.04	99.06			95.75	4.06		
	2σ	0.29	0.02	0.99	0.02	0.99	0.01	0.51	0.28	0.03		0.04				0.27	0.28		
Anorthite (L2)	12	43.14	b.d.	35.47	b.d.	0.49	b.d.	0.54	19.19	0.37	0.03	b.d.	99.24			96.46	3.36		
	2σ	0.28		0.66		0.27	0.00	0.38	0.35	0.02	0.00					0.16	0.16		
Chromite (L1) and (L2)	11	0.16	0.12	13.58	60.25	6.14	0.56	18.23	0.04	b.d.	b.d.	0.06	99.14						10.96
	2σ	0.15	0.05	0.64	0.98	0.15	0.02	0.23	0.02			0.02							0.72

2σ = standard deviation; b.d. = below detection.

distributions of silicate areas of L2 normalized to CI composition are shown in Fig. 11. The average REE composition shows a flat chondritic REE pattern (Fig. 11), although few compositions with REE-depleted patterns were observed in areas predominantly composed of olivine grains.

Oxygen Isotope Composition

Oxygen isotope compositions of duplicate analyses of L1 are in the range of other CBs (Clayton & Mayeda, 1999): $\delta^{17}O$ values are 1.889, −1.900; $\delta^{18}O$ values are 0.650, 0.590; $\Delta^{17}O$ values are −2.226, −2.206 (‰) (Fig. 12). Oxygen isotope compositions of duplicate analyses of L2 are $\delta^{17}O$ values of 0.095, 0.073; $\delta^{18}O$ values of 3.094, 3.052; $\Delta^{17}O$ values of 1.514, −1.514‰. This differs from L1; however, it is located along the CR-CH-CB trend line determined by Weisberg et al. (1995), to the ^{16}O-poor side of the other CBs on the three-isotope oxygen diagram (Clayton & Mayeda, 1999; Schrader et al., 2011) (Fig. 12).

DISCUSSION

Unusual Characteristics of Sierra Gorda 013 in Comparison with CBa Members

SG 013 was classified by Ivanova et al. (2019) as a CBa chondrite based on mineral chemistry and oxygen isotopic composition and is clearly similar to the CBa subgroup (Weisberg et al., 2001). However, it is an anomalous meteorite, several characteristics distinguish this meteorite from typical CBa meteorites (e.g., Bencubbin, Gujba), notably the occurrence of both chondritic and achondritic lithologies. The texture of the achondritic L2 is recrystallized and resembles the recrystallized matrix of the Fountain Hills CB-like chondrite (Weisberg & Ebel, 2009). Similarities and differences in some petrologic and chemical characteristics of these meteorites are summarized in Table 6.

Meteorites comprised of two texturally different lithologies have not been observed among CBa chondrites. Isheyevo (CH/CBb) also contains two lithologies, metal-poor and metal-rich, but they are both chondritic (Ivanova et al., 2008). In SG 013, it seems likely that both lithologies were initially in tight contact, perhaps as a lithified clastic breccia, but separated from each other on impact. The shock stages of L1 and L2 are similar (S2 stage); however, several areas in L1 are more shocked and correspond to S3–S4 stages, up to local impact melting (S5) (Stöffler et al., 1991) indicating heterogeneous effects of post-accretion impact event(s).

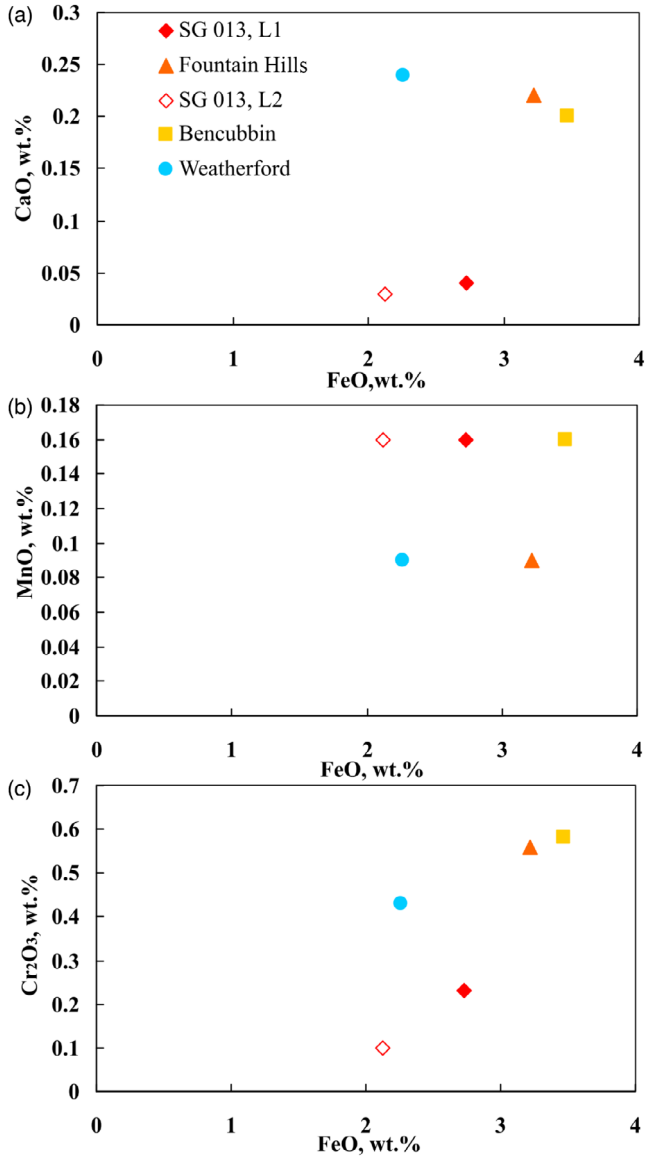

Fig. 6. Average composition of olivine from SG 013, lithologies 1 and 2 (L1 and L2) compare to that of Bencubbin, Weatherford (Weisberg et al., 2001), and Fountain Hills (Lauretta et al., 2009). a) FeO versus CaO. b) FeO versus MnO. c) FeO versus Cr_2O_3. (Color figure can be viewed at wileyonlinelibrary.com.)

L1 is clearly typical of CBa chondrites texturally—it contains abundant large Fe,Ni-metal globules, large chondrules, and their clast fragments, and does not contain matrix or matrix lumps. However, SG 013 contains porphyritic POP chondrules (~30%) in addition to BO and SO chondrules and separated POP grains in the peripheral area of the metal globules, while porphyritic chondrules are almost absent in CBa chondrites (Weisberg et al., 2001). Porphyritic chondrules in SG 013 are not classical in shape, but represent angular clasts of a rock with porphyritic texture (Fig. S2g, S2i, and S2k). In contrast, the CC chondrules that are typical of CBa and CBb chondrites are completely absent in SG 013. This characteristic of SG 013 is not typical for any other CBa chondrites nor the Fountain Hills chondrite (Weisberg & Ebel, 2009), which also contains abundant POP, BO, and CC chondrules, but not SO chondrules. This could indicate generally different conditions for the SG 013 and FH chondrule crystallization process compared to typical CBa chondrites like Gujba and Bencubbin.

Table 2. Representative analyses of metal and schreibersite from the lithologies L1 and L2 (wt%).

	Fe	Cr	Ni	S	P	Co	Total
Fe,Ni-metal (L1)	93.07	0.01	6.16	0.00	0.21	0.41	99.86
Schreibersite (L1)	48.33	0.06	35.94	0.02	15.43	0.11	99.90
Fe,Ni-metal (L2)	92.30	0.01	6.67	0.00	0.21	0.39	99.59
Fe,Ni-metal (L2)	85.95	0.01	12.57	0.00	0.05	0.30	98.90
Fe,Ni-metal (L2)	74.92	0.00	24.05	0.00	0.02	0.19	99.20

The L2 lithology is very different from all CB chondrites because of its achondritic texture (Table 6) and highly metamorphosed chondrites. L2 contains much less Fe,Ni-metal (~25 vol%) compared to L1 (~80 vol%) and other CBa chondrites (40–80 vol%, Weisberg & Ebel, 2009) (Table 6). A low abundance of Fe,Ni-metal (~26 vol%) was reported for the Fountain Hills CBa-like chondrite, a meteorite with other unusual characteristics (Weisberg & Ebel, 2009). Like L2 of SG 013, the Fountain Hills matrix also contains coarse anhedral olivine grains with smaller pyroxene, and anorthite, all surrounded by FeNi-metal (Weisberg & Ebel, 2009).

The olivine of both lithologies is homogeneous in composition, and based on major elements, it is similar to that in other CBa chondrites (Table 3; Fig. 3) (Weisberg et al., 2001). In both lithologies of SG 013, the contents of CaO and Cr_2O_3 in olivine are very low (0.03 ± 0.01 and 0.25 ± 0.14 wt%, respectively) and MnO content is high (0.16 ± 0.01 wt%) (Fig. 6) compared to olivine from other CBa chondrites (Weisberg & Ebel, 2009; Weisberg et al., 2001). In both lithologies, low-Ca pyroxene has similar compositions, which is typical for CBa chondrites, and, additionally, feldspar is alkali poor as in other CBa chondrites and suggests an Na-, K-poor bulk composition, as is characteristic of the CBa chondrites. However, based on Table 1, the Fe/Mn ratios of olivine and pyroxene, Fa of olivine, and Fs of low-Ca pyroxene of the L1

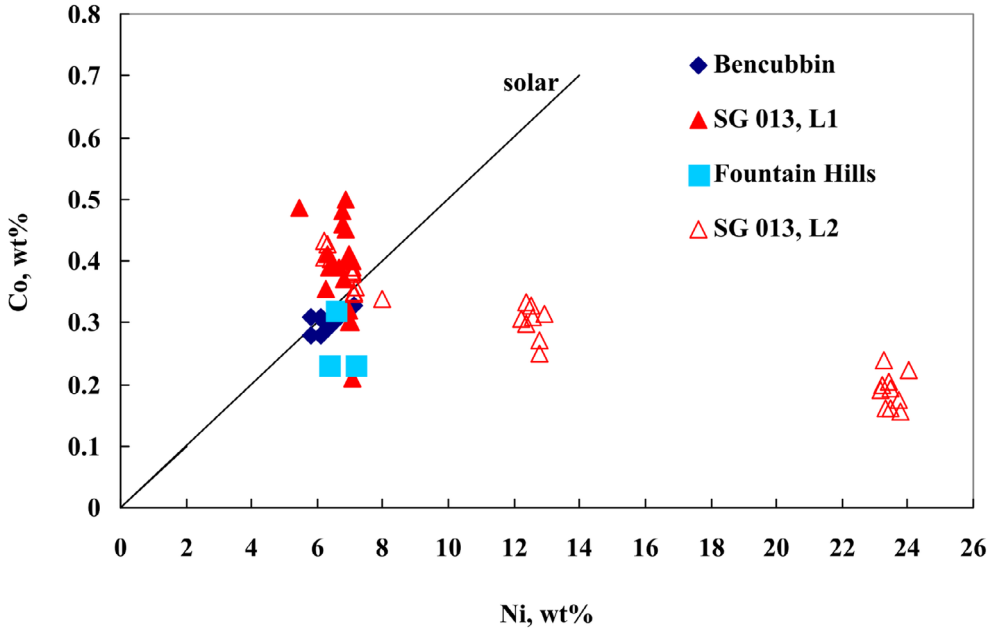

Fig. 7. Chemical composition of Fe,Ni-metal from SG 013, lithology 1 (L1) and lithology 2 (L2) compared to that of Bencubbin (Campbell et al., 2002) and Fountain Hills (Lauretta et al., 2009). (Color figure can be viewed at wileyonlinelibrary.com.)

Table 3. Representative analyses of sulfides (wt%) with formulae units from L1 of SG 013.

	S	V	Cr	Fe	Total	S	V	Cr	Fe	Sum
Daubreelite	44.65	0.01	35.43	19.92	100.01	4.00	0.00	1.96	1.02	6.98
V-daubreelite	44.09	6.22	29.74	18.54	98.59	4.00	0.36	1.66	0.97	6.98
V-brezinaite	44.14	10.64	36.90	6.27	98.26	4.00	0.62	2.05	0.33	7.00
Unknown V-sulfide	43.56	21.61	13.05	21.49	99.71	5.00	1.55	0.92	1.52	8.99

chondrules and clasts are generally higher than those of L2, indicating that L2 is slightly more reduced than L1. Unlike all CBa chondrites, SG 013 contains chromite and symplectites in chondrules of L1 and L2 also contains rare chromite among silicates. It is interesting to note that only one grain of spinel was found in the Fountain Hills chondrite (Weisberg & Ebel, 2009). The association of chromite with rutile and daubreelite in L1 also is not typical for CBa chondrites, which may be connected with the unusual characteristics of the SG 013 precursor material.

Similar to CBa, the metal of SG 013 L1 does not have an Ni-Co correlation (Fig. 7). The presence of low-Ni metal and high-Ni unzoned metal of different composition in L1 and L2 is also not typical for CBa chondrites, but is usual for CBb chondrites, for example, the CH/CBb chondrite Isheyevo (Ivanova et al., 2008), and for chondritic metal. Tiny glassy inclusions in the metal globules of L1 enriched in alkalis are not typical for CBa chondrites.

Sulfides are very rare in L1 of SG 013, similar to Fountain Hills (CBa-like; Weisberg & Ebel, 2009) and in contrast to the CBa chondrites (Table 6). All other CBa chondrites contain large mm-sized metal globules with small inclusions (blebs) of sulfide, daubreelite–troilite assemblages, and metal–troilite shock melt mixture that are usual components of CBa chondrites (e.g., Rubin et al., 2003; Srinivasan et al., 2017; Weisberg et al., 2001). The rare sulfide mineral association is unusual for CB chondrites, and besides daubreelite contacting with metal, also includes V-rich brezinaite and the unknown V-rich sulfide. Although Srinivasan et al. (2017) described V-rich troilite containing 1.8 wt% of V, V-daubreelite (V-6.2 wt%), V-brezinaite (V-10.6 wt%), and V-rich unknown sulfide (V-21.6 wt%) have not been reported in CBa chondrites before. The absence of any sulfides in L2 and their low abundance in L1 is an important difference between the lithologies of SG 013 and the material of other CBa chondrites, and resembles Fountain Hills (Weisberg & Ebel, 2009). This peculiarity could be connected with evaporation of sulfur in the impact plume and is discussed below.

The oxygen isotopic composition of L1 and L2 (Fig. 12) is different but follows the CR chondrite

Table 4. Bulk elemental abundances of Fe,Ni-metal globules from lithology 1.

		1	SD	2	SD	3	SD	4	SD	5	SD	6	SD	D.L.
Si	(wt%)	bdl		bdl		bdl		bdl		bdl		bdl		0.03
P	(wt%)	0.14	0.01	0.13	0.01	0.16	0.02	0.15	0.02	0.17	0.01	0.20	0.01	0.003
S	(wt%)	0.03	0.01	0.05	0.01	0.06	0.02	0.08	0.02	0.08	0.02	0.06	0.02	0.04
Ti	(ppm)	51	15	52	17	26	6	24	5	21	3	16	2	3
V	(ppm)	0.40	0.13	1.0	2.4	0.3	0.2	0.2	0.1	0.3	0.1	0.5	0.2	0.02
Cr	(ppm)	0.090	0.002	315	552	88	23	139	96	157	127	131	126	0.7
Fe	(wt%)	93.00	0.10	93.01	0.10	93.26	0.15	93.26	0.11	93.33	0.03	93.36	0.01	
Co	(wt%)	0.33	0.004	0.32	0.003	0.32	0.005	0.32	0.002	0.32	0.003	0.32	0.002	0.1
Ni	(wt%)	6.66	0.10	6.64	0.12	6.40	0.15	6.40	0.11	6.33	0.03	6.31	0.09	0.2
Cu	(ppm)	47	1	49	1	44	2	45	3	42	0	41	1	0.03
Zn	(ppm)	0.3	0.1	0.6	0.1	0.3	0.1	0.2	0.1	0.2	0.0	0.3	0.1	0.02
Ga	(ppm)	2.3	0.1	2.4	0.1	2.0	0.1	2.0	0.2	1.8	0.1	1.8	0.0	0.02
Ge	(ppm)	bdl		bdl		bdl		bdl		bdl		bdl		0.02
As	(ppm)	4.4	0.46	3.3	0.46	3.3	0.30	3.5	0.24	3.5	0.13	3.8	0.26	0.07
Mo	(ppm)	4.3	0.5	4.91	0.5	7.6	2.7	8.3	3.6	9.8	1.6	12.7	2.0	0.2
Ru	(ppm)	1.94	0.3	2.26	0.33	4.79	1.8	5.37	2.5	6.73	0.7	8.03	0.9	0.03
Rh	(ppm)	0.60	0.11	0.60	0.11	1.41	0.50	1.51	0.59	1.90	0.16	2.19	0.17	0.02
Pd	(ppm)	3.08	0.37	2.98	0.37	3.85	0.53	3.95	0.75	4.34	0.28	4.59	0.22	0.02
Sb	(ppm)	0.08	0.03	0.18	0.03	0.06	0.02	0.08	0.03	0.06	0.02	0.04	0.01	0.02
W	(ppm)	0.16	0.04	0.19	0.04	0.90	0.71	1.22	1.10	1.59	0.33	2.94	0.80	0.04
Re	(ppm)	0.06	0.04	0.09	0.04	0.42	0.30	0.45	0.39	0.66	0.27	1.23	0.43	0.01
Os	(ppm)	0.23	0.14	0.55	0.14	4.22	3.22	5.91	5.25	7.97	1.86	12.94	3.50	0.05
Ir	(ppm)	0.35	0.16	0.58	0.16	3.59	2.43	4.25	3.26	5.82	1.12	8.87	1.95	0.01
Pt	(ppm)	1.30	0.39	1.70	0.39	5.56	2.90	6.28	3.60	8.65	1.04	10.49	1.57	0.05
Au	(ppm)	0.59	0.05	0.53	0.05	0.56	0.06	0.62	0.07	0.63	0.06	0.56	0.05	0.02

D.L. = detection limit; bdl = below detection; SD = standard deviation.
Metal globules: #1—points 26–33; #2—points 34–43; #3—points 44–52; #4—points 53–61; #5—points 62–66; #6—points 67–72 (Fig. S1a).

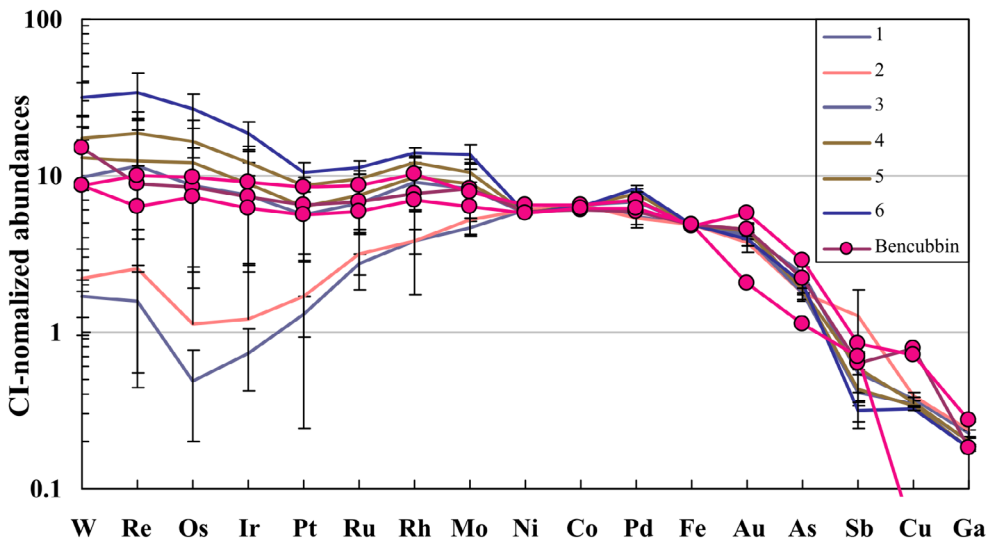

Fig. 8. Average siderophile element composition of metal globules from L1 of SG 013 compared to the metal composition of the Bencubbin CBa chondrite (Campbell et al., 2002) normalized to CI composition (Anders & Grevesse, 1989). Each line belongs to average composition of every metal globule. Standard deviations are shown as black bars. (Color figure can be viewed at wileyonlinelibrary.com.)

mixing line described by Weisberg et al. (1995). Despite the fact that both lithologies of SG 013 are different in texture, modal composition, and mineralogy, they were formed in the CBa reservoir based on oxygen isotopic compositions and mineral chemistry. Several important differences between SG 013 and other CBa chondrites

Table 5. Bulk major (in wt%) and trace (in ppm) element abundances with standard deviation of silicate chondrules (1–11) from the lithology 1 and silicate areas (94–111) and bulk raster of lithology 2 of SG 013 obtained by LA-ICP-MS.

	Lithology 1																						
wt%	1-SO	SD	2-SO	SD	3-SO	SD	4-POP	SD	5-BO	SD	6-BO	SD	7-PP	SD	8-POP	SD	9-POP	SD	10-POP	SD	11-SO	SD	D.L.
SiO_2	50.4	2.39	49.2	0.18	48.5	0.35	39.7	0.30	46.6	0.55	46.6	0.62	56.3	1.19	50.4	7.50	48.5	2.29	41.4	1.42	52.0	0.60	0.0050
TiO_2	0.17	0.05	0.18	0.02	0.12	0.009	0.04	0.01	0.11	0.01	0.11	0.01	0.20	0.03	0.12	0.06	0.11	0.03	0.05	0.02	0.16	0.01	0.0001
Al_2O_3	7.21	1.34	7.92	0.26	7.77	0.380	0.25	0.21	9.93	0.56	10.3	0.55	5.28	2.33	2.00	1.45	1.72	1.08	0.39	0.25	3.27	0.30	0.001
FeO_T	2.01	0.22	1.89	0.06	1.93	0.13	4.81	1.09	1.84	0.10	1.82	0.11	3.19	0.53	3.51	0.39	3.02	0.28	4.01	0.42	2.55	0.11	0.0001
MnO	0.16	0.02	0.14	0.00	0.14	0.003	0.19	0.00	0.12	0.00	0.12	0.00	0.16	0.02	0.19	0.01	0.19	0.01	0.18	0.01	0.18	0.00	0.000004
MgO	35.0	0.86	33.6	0.80	34.7	0.69	54.7	1.32	31.9	1.37	31.3	1.22	27.9	4.04	42.1	9.38	44.7	3.97	52.8	2.27	38.9	1.03	0.0005
CaO	4.98	0.79	6.99	0.46	6.78	0.47	0.36	0.22	9.36	0.60	9.55	0.51	6.89	3.34	1.68	1.11	1.73	1.03	0.65	0.32	2.97	0.19	0.002
Na_2O	0.12	0.05	0.11	0.01	0.09	0.005	0.01	0.01	0.15	0.01	0.15	0.01	0.10	0.04	0.03	0.02	0.03	0.02	0.50	0.61	0.05	0.01	0.002
K_2O	0.004	0.001	bdl		bdl		bdl		0.005	0.001	0.005	0.000	bdl		bdl		bdl		bdl		bdl		0.002
P_2O_5	0.002	0.001	0.002	0.00	0.003	0.001	0.002	0.001	0.003	0.004	0.002	0.001	0.003	0.001	0.003	0.001	0.002	0.001	0.003	0.001	0.001	0.0003	0.0001
Li	2.8	0.9	1.8	0.2	1.7	0.4	2.5	1.1	2.4	0.4	2.2	0.4	2.1	0.2	2.5	0.3	2.4	0.3	2.7	0.9	3.3	0.5	0.1
Be	0.12	0.02	0.14	0.01	0.14	0.03	0.01	0.01	0.16	0.03	0.17	0.02	0.10	0.03	bld		bld		bld		0.05	0.00	0.02
B	2.81	4.84	0.52	0.32	1.06	0.39	3.15	2.27	1.68	0.9	1.94	1.10	2.90	1.31	6.10	2.25	3.36	1.32	11.95	7.12	4.11	1.68	0.03
Sc	23.6	5.2	33.3	2.80	25.0	1.9	10.2	0.9	29.4	3.7	28.8	2.9	20.2	1.8	16.3	4.3	11.2	2.0	9.9	2.2	14.9	0.7	0.2
V	173	47	150	26	124	6	109	7	125	12	123	9	143	22	137	24	146	18	98	17	153	7	0.007
Cr	7510	3465	4079	1976	3107	501	3308	370	3061	1120	2999	1083	5728	428	4859	1554	5604	1287	2328	1148	4848	474	0.04
Co	9	14	2	0.6	7	4	40	26	7	2.3	9	3	36	7	23	8	13	2	34	19	11	6	0.01
Ni	246	441	48	26	168	107	1095	1048	143	75	178	90	916	228	517	176	307	79	854	625	240	184	0.06
Cu	0.3	0.2	0.2	0.1	0.5	0.3	0.4	0.2	0.3	0.1	0.4	0.0	1.8	0.7	0.6	0.4	0.9	0.6	0.7	0.1	1.9	0.8	0.2
Zn	0.40	0.02	0.42	0.03	0.39	0.09	0.33	0.02	0.40	0.1	0.42	0.08	0.37	0.01	0.41	0.12	0.47	0.09	1.07	0.42	0.54	0.19	0.02
Ga	0.15	0.02	0.36	0.21	0.23	0.02	bdl		0.30	0.01	0.31	0.01	0.24	0.11	0.04	0.02	0.07	0.03	0.16	0.12	0.11	0.02	0.01
Ge	bdl		bdl		bdl		bdl		0.03	0.00	bdl		bdl		bdl		bdl		bdl		bdl		0.02
As	0.04	0.01	0.08	0.07	0.06	0.01	0.06	0.01	0.07	0.01	0.06	0.00	0.06	0.01	0.04	0.00	0.04	0.01	0.06	0.01	0.05	0.01	0.003
Se	bdl		0.6	0.1	0.5	0.2	0.5	0.2	0.9	0.1	0.9	0.2	1.2	0.6	0.8	0.1	0.4	0.000	0.3	0.1	0.4	0.2	0.1
Rb	0.07	0.01	0.04	0.01	0.04	0.00	0.07	0.02	0.06	0.02	0.05	0.01	0.03	0.00	bdl		bdl		2.34	1.96	0.05	0.03	0.02
Sr	39.4	9.9	44.9	3.8	49.6	2.7	1.1	1.2	69.5	5.6	72.8	5.4	40.8	21.6	10.4	8.9	9.9	8.2	5.4	5.3	20.5	2.5	0.004
Y	4.30	1.13	8.43	1.21	4.98	0.64	0.62	0.21	6.79	0.8	6.69	0.55	6.86	2.15	2.41	1.47	2.89	1.19	0.72	0.55	3.58	0.20	0.003
Zr	12.01	2.74	21.77	3.52	14.70	1.52	2.09	0.618	18.34	1.7	18.15	1.45	17.80	7.49	4.96	2.41	6.68	3.01	3.48	1.07	11.57	0.61	0.004
Nb	0.55	0.10	0.73	0.04	1.00	0.09	0.14	0.07	0.58	0.10	0.59	0.12	0.47	0.21	0.16	0.04	0.24	0.04	0.12	0.05	0.88	0.09	0.0005
Mo	0.12	0.11	0.23	0.08	0.34	0.04	0.05	0.02	0.13	0.112	0.19	0.127	0.26	0.22	0.06	0.02	0.04	0.01	0.12	0.02	0.02	0.01	0.01
Ag	0.009	0.004	0.005	0.001	0.006	0.004	0.007	0.008	0.029	0.046	0.007	0.001	0.004	0.001	0.003	0.001	0.005	0.001	0.008	0.003	0.006	0.000	0.001
Cd	0.067	0.021	0.059	0.019	0.059	0.014	0.059	0.006	0.085	0.035	0.053	0.009	0.061	0.019	0.207	0.073	0.180	0.066	0.062	0.014	0.060	0.023	0.002
In	0.002	0.002	bdl		bdl		bdl		bd1		bdl		bdl		bdl		bdl		bd1		bdl		0.0009

	Lithology 1																						
ppm	1-SO	SD	2-SO	SD	3-SO	SD	4-POP	SD	5-BO	SD	6-BO	SD	7-PP	SD	8-POP	SD	9-POP	SD	10-POP	SD	11-SO	SD	D.L.
Sn	0.058	0.034	0.025	0.009	0.023	0.008	0.034	0.019	0.042	0.010	0.047	0.010	0.030	0.017	0.044	0.031	0.020	0.007	0.274	0.173	0.037	0.038	0.004
Sb	0.012	0.003	0.219	0.400	0.016	0.003	0.013	0.002	0.023	0.006	0.018	0.005	0.012	0.002	0.027	0.009	0.019	0.007	0.028	0.013	0.010	0.000	0.001
Cs	bdl		bdl		bdl		bdl		bdl		bdl		bdl		bdl		bdl		bdl		bdl		0.02
Ba	15.6	3.9	17.9	1.2	18.2	0.7	0.4	0.5	25.1	0.745	25.8	0.3	12.1	6.1	3.5	3.2	3.2	2.7	1.1	0.6	7.1	0.6	0.001
La	1.14	0.21	1.66	0.12	1.72	0.10	0.06	0.05	2.25	0.10	2.28	0.07	1.50	0.76	0.27	0.17	0.32	0.23	0.10	0.05	0.77	0.04	0.002
Ce	3.43	0.60	5.98	0.61	5.20	0.33	0.30	0.28	7.08	0.27	7.10	0.06	5.56	2.62	0.71	0.39	1.11	0.86	0.31	0.22	2.45	0.15	0.0003
Pr	0.39	0.09	0.71	0.10	0.69	0.06	0.04	0.03	1.03	0.08	1.02	0.06	0.85	0.44	0.09	0.05	0.15	0.12	0.04	0.03	0.30	0.01	0.0003
Nd	1.65	0.49	3.32	0.48	3.27	0.43	0.18	0.15	4.79	0.48	4.75	0.21	4.22	2.15	0.47	0.28	0.77	0.63	0.21	0.17	1.40	0.11	0.001
Sm	0.46	0.14	0.97	0.15	0.89	0.10	0.05	0.04	1.29	0.14	1.27	0.10	1.25	0.64	0.16	0.10	0.26	0.19	0.06	0.05	0.44	0.04	0.001
Eu	0.31	0.08	0.35	0.03	0.39	0.03	0.01	0.01	0.53	0.03	0.54	0.02	0.29	0.14	0.08	0.07	0.07	0.06	0.01	0.01	0.15	0.02	0.001
Gd	0.60	0.18	1.31	0.21	0.99	0.14	0.07	0.05	1.43	0.17	1.42	0.08	1.30	0.58	0.27	0.18	0.40	0.25	0.09	0.10	0.59	0.03	0.003
Tb	0.11	0.03	0.22	0.04	0.15	0.02	0.01	0.01	0.22	0.02	0.21	0.02	0.21	0.09	0.05	0.03	0.07	0.03	0.01	0.01	0.10	0.01	0.0008
Dy	0.74	0.22	1.48	0.23	0.95	0.12	0.09	0.05	1.32	0.16	1.26	0.11	1.32	0.48	0.38	0.24	0.49	0.23	0.11	0.09	0.66	0.05	0.001

Table 5. *Continued*. Bulk major (in wt%) and trace (in ppm) element abundances with standard deviation of silicate chondrules (1–11) from the lithology 1 and silicate areas (94–111) and bulk raster of lithology 2 of SG 013 obtained by LA-ICP-MS.

	Lithology 1																					
ppm	1-SO	SD	2-SO	SD	3-SO	SD	4-POP	SD	5-BO	SD	6-BO	SD	7-PP	SD	8-POP	SD	9-POP	SD	10-POP	SD	11-SO	SD	D.L.
Ho	0.16	0.04	0.31	0.04	0.18	0.02	0.02	0.01	0.24	0.03	0.24	0.02	0.25	0.07	0.09	0.05	0.10	0.04	0.02	0.02	0.14	0.00	0.0002
Er	0.49	0.12	0.89	0.12	0.50	0.05	0.08	0.02	0.63	0.09	0.61	0.08	0.70	0.17	0.29	0.17	0.33	0.11	0.09	0.06	0.39	0.02	0.0009
Tm	0.079	0.019	0.128	0.017	0.071	0.009	0.015	0.003	0.083	0.013	0.078	0.011	0.092	0.019	0.045	0.025	0.047	0.015	0.017	0.007	0.055	0.006	0.0008
Yb	0.55	0.12	0.76	0.09	0.42	0.04	0.12	0.01	0.44	0.05	0.44	0.04	0.57	0.09	0.31	0.15	0.31	0.08	0.12	0.04	0.36	0.03	0.0009
Lu	0.09	0.02	0.13	0.01	0.06	0.01	0.03	0.00	0.07	0.01	0.06	0.01	0.09	0.01	0.05	0.02	0.05	0.01	0.03	0.01	0.06	0.01	0.0005
Hf	0.32	0.08	0.64	0.11	0.48	0.05	0.06	0.02	0.64	0.09	0.60	0.06	0.55	0.21	0.16	0.09	0.19	0.09	0.09	0.03	0.30	0.03	0.002
Ta	0.030	0.006	0.048	0.005	0.060	0.007	0.003	0.000	0.037	0.005	0.037	0.006	0.032	0.013	0.011	0.004	0.014	0.002	0.028	0.028	0.052	0.004	0.0007
W	0.162	0.207	0.444	0.133	0.578	0.277	0.007	0.005	0.241	0.267	0.297	0.341	0.029	0.012	0.007	0.004	0.029	0.016	0.018	0.013	0.004	0.002	0.003
Re	0.004	0.004	0.003	0.003	0.005	0.003	0.008	0.005	0.006	0.005	0.003	0.001	0.044	0.016	0.008	0.008	0.007	0.007	0.019	0.003	0.012	0.011	0.0003
Os	0.002	0.002	bdl		0.003	0.001	0.033	0.032	0.004	0.001	0.004	0.001	0.170	0.166	0.018	0.005	0.023	0.022	0.102	0.033	0.005	0.002	0.002
Ir	bdl		bdl		bdl		0.166	0.000	0.004	0.001	0.004	0.001	0.137	0.151	0.009	0.005	0.032	0.027	0.046	0.009	0.003	0.002	0.002
Pt	0.032	0.026	0.022	0.005	0.024	0.013	0.046	0.019	0.069	0.042	0.044	0.022	0.347	0.320	0.125	0.116	0.065	0.023	0.287	0.145	0.120	0.112	0.005
Au	bdl		bdl		bdl		bdl		bdl		bdl		bdl		bdl		bdl		bdl		bdl		0.002
Tl	0.001	0.000	0.002	0.000	bdl		bdl		bdl		bdl		bdl		bdl		bdl		bdl		bdl		0.0007
Pb	0.076	0.011	0.132	0.033	0.105	0.022	0.020	0.019	0.074	0.017	0.063	0.005	0.053	0.014	0.081	0.047	0.057	0.015	0.244	0.139	0.140	0.055	0.0007
Bi	0.003	0.001	0.005	0.003	0.002	0.001	0.004	0.004	0.003	0.001	0.002	0.000	0.003	0.001	0.006	0.003	0.006	0.002	0.005	0.003	0.002	0.001	0.0006
Th	0.099	0.026	0.150	0.008	0.145	0.011	0.012	0.005	0.067	0.010	0.061	0.005	0.065	0.019	0.031	0.012	0.036	0.011	0.020	0.013	0.182	0.059	0.0003
U	0.029	0.006	0.045	0.007	0.045	0.002	0.010	0.006	0.026	0.002	0.025	0.001	0.027	0.007	0.008	0.002	0.012	0.004	0.019	0.020	0.055	0.017	0.0002

Lithology 2																						
wt%	94	95	96	97	98	99	100	101	102	103	104	105	106	107	108	109	110	111	Raster	Average	SD	D.L.
SiO_2	44.6	48.8	59.1	46.5	48.0	54.6	42.8	43.1	40.2	53.7	40.8	41.2	40.4	39.9	40.0	41.5	50.3	58.7	42.2	46.1	6.41	0.0050
TiO_2	0.15	0.15	0.20	0.08	0.11	0.20	0.08	0.07	0.01	0.17	0.02	0.04	0.01	0.02	0.02	bdl	0.12	0.21	0.10	0.10	0.07	0.0001
Al_2O_3	4.24	2.12	0.82	2.04	2.76	1.63	1.63	1.97	0.01	2.40	0.11	0.64	0.02	0.22	0.03	bdl	2.21	0.98	1.90	1.43	1.16	0.001
FeO_T	13.8	8.25	3.11	3.13	3.73	6.37	7.44	2.93	2.58	3.63	2.37	4.88	2.81	3.72	2.79	2.96	2.77	2.86	15.3	5.02	3.76	0.0001
MnO	0.14	0.16	0.19	0.17	0.17	0.18	0.16	0.17	0.18	0.18	0.18	0.18	0.18	0.18	0.18	0.18	0.17	0.19	0.15	0.17	0.01	0.000004
MgO	33.0	38.2	35.5	46.3	42.8	34.6	46.4	49.5	56.9	37.9	56.4	52.4	56.4	55.7	56.9	55.3	42.9	35.8	38.5	45.9	8.83	0.0005
CaO	3.88	2.18	1.10	1.69	2.37	2.32	1.39	2.27	0.10	1.94	0.14	0.62	0.09	0.24	0.10	bdl	1.44	1.27	1.75	1.38	1.04	0.002
Na_2O	0.14	0.05	0.04	0.06	0.04	0.03	0.04	0.03	bdl	0.03	bdl	0.02	bdl	bdl	bdl	0.05	0.05	0.01	0.04	0.04	0.03	0.002
K_2O	0.012	0.007	0.015	0.020	0.002	0.003	0.005	0.002	bdl	bdl	bdl	bdl	bdl	bdl	bdl	0.019	0.010	bdl	0.008	0.009	0.01	0.002
P_2O_5	0.069	0.035	0.004	0.006	0.010	0.015	0.021	0.004	0.003	0.008	0.002	0.027	0.003	0.003	0.002	0.004	0.004	0.003	0.057	0.015	0.02	0.0001
ppm																						
Li	5.6	3.4	6.0	6.2	2.5	3.4	3.6	2.9	2.6	2.4	2.5	2.7	2.4	2.7	2.4	9.0	8.1	2.3	5.0	4.00	2.07	0.1
Be	0.06	0.06	0.07	0.13	0.09	bdl	0.03	0.06	0.04	0.06	bdl	bdl	bdl	bdl	bdl	bdl	bdl	bdl	0.04	0.06	0.03	0.02
B	26.67	19.12	1.14	3.29	3.82	8.71	11.89	2.26	1.32	2.97	0.73	3.63	0.67	1.57	0.77	1.98	1.89	1.56	32.35	6.65	9.34	0.03
Sc	14.0	14.6	15.4	6.5	11.2	18.5	9.0	8.1	3.4	15.3	3.9	5.8	3.4	4.5	5.4	bdl	1.4	17.9	10.0	9.3	5.46	0.2
V	97	110	126	87	102	137	76	82	63	136	62	68	73	79	75	60	88	134	90	92	25.7	0.007
Cr	2507	3181	5093	2174	2680	4742	1900	1599	826	5728	1268	1340	1768	1389	1708	884	2535	5237	2677	2591	1527	0.04
Co	340	183	20	26	41	102	120	22	9	36	6	44	8	22	9	14	17	15	346	73	106	0.01
Ni	14573	4368	402	746	909	2343	4142	424	153	892	145	1178	176	501	129	451	331	212	7789	2098	3619	0.06
Cu	12.3	4.6	0.7	2.6	4.7	5.0	3.1	1.8	0.3	4.0	0.2	3.3	0.4	0.4	0.2	0.7	1.1	1.0	8.6	2.9	3.21	0.2
Zn	1.02	1.12	1.42	1.69	1.39	1.34	0.48	1.12	1.10	0.86	1.39	1.53	1.79	1.53	1.56	1.82	0.79	0.96	3.18	1.37	0.56	0.02
Ga	0.63	0.18	0.03	0.12	0.08	0.07	0.07	0.12	bdl	0.08	0.02	0.05	bdl	0.02	bdl	0.08	0.04	0.03	0.21	0.11	0.15	0.01
Ge	bdl	bdl	bdl	bdl	bdl	bdl	bdl	bdl	bdl	bdl	bdl	bdl	bdl	bdl	bdl	bdl	bdl	bdl	bdl	bdl		0.02
As	0.63	0.15	0.03	0.08	0.09	0.09	0.09	0.05	0.06	0.04	0.04	0.11	0.04	0.05	0.04	0.09	0.06	0.04	0.36	0.11	0.15	0.003
Se	bdl	bdl	bdl	bdl	bdl	bdl	bdl	bdl	bdl	bdl	bdl	bdl	bdl	bdl	bdl	bdl	bdl	bdl	3.2	3.18		0.1
Rb	0.31	0.07	0.14	0.31	0.02	0.04	0.08	0.02	bdl	bdl	bdl	bdl	bdl	bdl	bdl	0.18	0.13	bdl	0.08	0.12	0.10	0.02

Table 5. *Continued*. Bulk major (in wt%) and trace (in ppm) element abundances with standard deviation of silicate chondrules (1–11) from the lithology 1 and silicate areas (94–111) and bulk raster of lithology 2 of SG 013 obtained by LA-ICP-MS.

Lithology 2																						
wt%	94	95	96	97	98	99	100	101	102	103	104	105	106	107	108	109	110	111	Raster	Average	SD	D.L.
Sr	27.6	15.4	0.6	10.4	16.2	21.2	11.9	12.0	0.1	10.7	0.5	4.4	0.2	1.3	0.0	bdl	11.4	1.6	20.7	9.23	8.64	0.004
Y	4.41	3.01	4.49	2.24	2.66	4.47	1.77	2.94	0.07	3.75	0.17	0.75	0.17	0.31	0.16	bdl	2.35	4.47	2.32	2.25	1.66	0.003
Zr	11.92	5.86	6.24	5.67	7.05	8.92	4.69	8.54	0.13	7.19	1.00	2.11	1.69	1.16	1.02	0.13	4.80	6.28	5.57	4.74	3.35	0.004
Nb	0.51	0.28	0.29	0.35	0.50	0.35	0.38	0.43	0.00	0.35	0.16	0.15	0.30	0.10	0.18	0.02	0.30	0.24	0.30	0.27	0.14	0.0005
Mo	1.18	0.26	0.10	0.02	0.20	0.22	0.39	0.05	0.02	0.06	0.02	0.33	0.04	0.04	0.03	0.09	1.30	0.39	2.40	0.38	0.61	0.01
Ag	bdl	bdl	bdl	bdl	bdl	bdl	bdl	bdl	bdl	bdl	bdl	bdl	bdl	bdl	bdl	bdl	bdl	bdl	bdl	bdl		0.001
Cd	0.121	0.111	0.085	0.069	0.060	0.130	0.082	0.065	0.052	0.039	0.048	0.090	0.051	0.041	0.045	0.017	0.025	0.048	0.022	0.063	0.03	0.002
In	0.002	bdl	bdl	bdl	bdl	bdl	bdl	bdl	bdl	bdl	bdl	bdl	bdl	bdl	bdl	bdl	bdl	bdl	0.001	0.002	0.0004	0.0009

Lithology 2																						
ppm	94	95	96	97	98	99	100	101	102	103	104	105	106	107	108	109	110	111	Raster	Average	SD	D.L.
Sn	0.027	0.033	0.009	0.057	0.028	0.019	0.021	0.030	0.022	0.027	0.030	0.036	0.034	0.048	0.030	bdl	0.007	0.026	0.055	0.030	0.013	0.004
Sb	0.012	0.016	bdl	0.013	0.009	0.018	0.008	0.022	0.009	0.014	0.010	0.013	0.005	0.011	0.004	0.001	0.008	0.013	0.006	0.011	0.005	0.001
Cs	bdl	bdl	bdl	bdl	bdl	bdl	bdl	bdl	bdl	bdl	bdl	bdl	bdl	bdl	bdl	bdl	bdl	bdl	bdl	bdl		0.02
Ba	9.0	3.6	0.2	3.7	6.0	2.0	3.6	4.3	0.0	3.8	0.2	1.5	0.0	0.5	0.0	0.0	3.9	0.5	3.7	2.5	2.477	0.001
La	0.796	0.269	0.123	0.354	0.505	0.363	0.291	0.562	0.002	0.362	0.035	0.142	0.033	0.066	0.013	bdl	0.258	0.108	0.328	0.256	0.216	0.002
Ce	2.490	0.699	0.371	0.963	1.561	1.068	0.796	1.805	0.009	1.006	0.092	0.445	0.095	0.177	0.058	0.034	0.584	0.325	0.946	0.712	0.675	0.0003
Pr	0.327	0.083	0.043	0.141	0.180	0.153	0.091	0.258	0.001	0.128	0.011	0.052	0.010	0.020	0.005	bdl	0.081	0.042	0.117	0.097	0.090	0.0003
Nd	1.815	0.456	0.330	0.626	0.812	0.736	0.511	1.381	0.006	0.591	0.023	0.282	0.026	0.104	0.022	0.080	0.431	0.260	0.584	0.478	0.476	0.001
Sm	0.610	0.163	0.143	0.123	0.258	0.239	0.157	0.400	bdl	0.254	bdl	0.091	0.006	0.033	0.006	bdl	0.157	0.143	0.190	0.186	0.152	0.001
Eu	0.231	0.078	bdl	0.104	0.130	0.053	0.071	0.100	bdl	0.092	bdl	0.035	bdl	0.014	bdl	bdl	0.092	0.011	0.082	0.084	0.056	0.001
Gd	0.700	0.286	0.297	0.289	0.380	0.437	0.243	0.537	bdl	0.387	0.018	0.131	0.016	0.034	0.011	0.008	0.386	0.345	0.298	0.267	0.199	0.003
Tb	0.113	0.049	0.056	0.055	0.074	0.086	0.039	0.097	bdl	0.073	bdl	0.022	0.005	0.007	bdl	bdl	0.057	0.076	0.053	0.058	0.031	0.0008
Dy	0.795	0.481	0.724	0.390	0.453	0.755	0.321	0.561	0.007	0.565	0.032	0.117	0.012	0.057	0.015	0.008	0.369	0.626	0.385	0.351	0.279	0.001
Ho	0.169	0.109	0.194	0.073	0.101	0.161	0.068	0.117	bdl	0.140	0.007	0.030	0.005	0.015	0.005	0.012	0.105	0.173	0.086	0.087	0.064	0.0002
Er	0.489	0.344	0.552	0.267	0.296	0.517	0.228	0.291	0.005	0.436	0.032	0.099	0.023	0.040	0.029	0.028	0.352	0.537	0.279	0.255	0.195	0.0009
Tm	0.063	0.062	0.094	0.042	0.050	0.082	0.030	0.042	bdl	0.074	bdl	0.018	0.007	0.011	0.007	0.001	0.070	0.078	0.043	0.046	0.030	0.0008
Yb	0.412	0.359	0.606	0.214	0.291	0.538	0.231	0.248	0.043	0.505	0.063	0.112	0.050	0.070	0.055	0.061	0.369	0.591	0.289	0.269	0.195	0.0009
Lu	0.066	0.067	0.116	0.041	0.050	0.098	0.036	0.038	0.011	0.076	0.016	0.019	0.017	0.020	0.018	0.027	0.048	0.107	0.050	0.048	0.032	0.0005
Hf	0.399	0.180	0.273	0.181	0.210	0.324	0.122	0.283	0.008	0.274	0.028	0.075	0.042	0.039	0.025	0.006	0.200	0.222	0.175	0.161	0.119	0.002
Ta	0.037	0.019	0.010	0.024	0.027	0.024	0.018	0.032	bdl	0.020	0.006	0.010	0.005	0.007	0.007	0.003	0.018	0.018	0.017	0.017	0.010	0.0007
W	0.273	0.081	0.003	0.013	0.017	0.021	0.298	0.023	bdl	bdl	bdl	0.087	bdl	bdl	bdl	bdl	bdl	0.018	0.210	0.095	0.112	0.003
Re	0.091	0.047	0.022	0.012	0.015	0.053	0.082	0.017	0.001	0.012	0.010	0.039	0.007	0.010	0.001	0.044	0.126	0.042	0.400	0.054	0.090	0.0003
Os	1.625	0.279	0.004	0.000	0.158	0.086	0.279	0.029	0.011	0.056	0.003	0.197	0.005	0.077	0.010	bdl	0.467	0.206	5.215	0.484	1.240	0.002
Ir	1.521	0.309	0.022	0.011	0.102	0.058	0.286	0.023	0.013	0.021	0.006	0.145	0.005	0.056	0.006	bdl	0.107	0.046	5.181	0.440	1.234	0.002
Pt	2.046	2.233	0.424	0.421	0.965	0.978	1.092	0.696	0.055	0.704	0.152	1.227	0.101	0.174	0.051	0.295	0.609	0.371	12.272	1.309	2.727	0.005
Au	0.141	0.075	0.019	bdl	0.042	0.013	0.049	0.041	0.005	0.007	bdl	0.009	0.015	0.007	bdl	0.036	0.060	0.020	0.240	0.049	0.062	0.002
Tl	0.002	bdl	0.002	bdl	bdl	bdl	bdl	bdl	bdl	bdl	bdl	bdl	bdl	bdl	bdl	bdl	bdl	bdl	bdl	bdl		0.0007
Pb	1.513	0.345	0.219	0.318	0.360	0.225	0.180	0.190	0.151	0.345	0.349	0.304	0.219	0.236	0.221	0.833	0.103	0.277	0.979	0.388	0.350	0.0007
Bi	0.004	0.003	0.003	0.002	0.003	0.003	0.004	0.002	0.001	0.001	0.002	0.002	0.001	0.002	0.002	bdl	bdl	0.001	0.003	0.002	0.001	0.0006
Th	0.089	0.046	0.047	0.074	0.056	0.063	0.055	0.056	0.000	0.068	0.013	0.024	0.018	0.011	0.010	0.009	0.066	0.071	0.048	0.043	0.027	0.0003
U	0.027	0.010	0.020	0.013	0.020	0.018	0.012	0.016	0.001	0.014	0.010	0.009	0.009	0.005	0.007	bdl	0.012	0.017	0.015	0.013	0.006	0.0002

D.L. = detection limit. bdl = below detection limit; Chondrules: #1—points 31–36; #2—points 37–41; #3—42–50; #4—51–55; #5—points 56–61; #6—points 62–64; #7—points 65–68; #8—points 69–73; #9—points 74–77; #10—points 78–80; #11—points 81–85 (Fig. S1b).

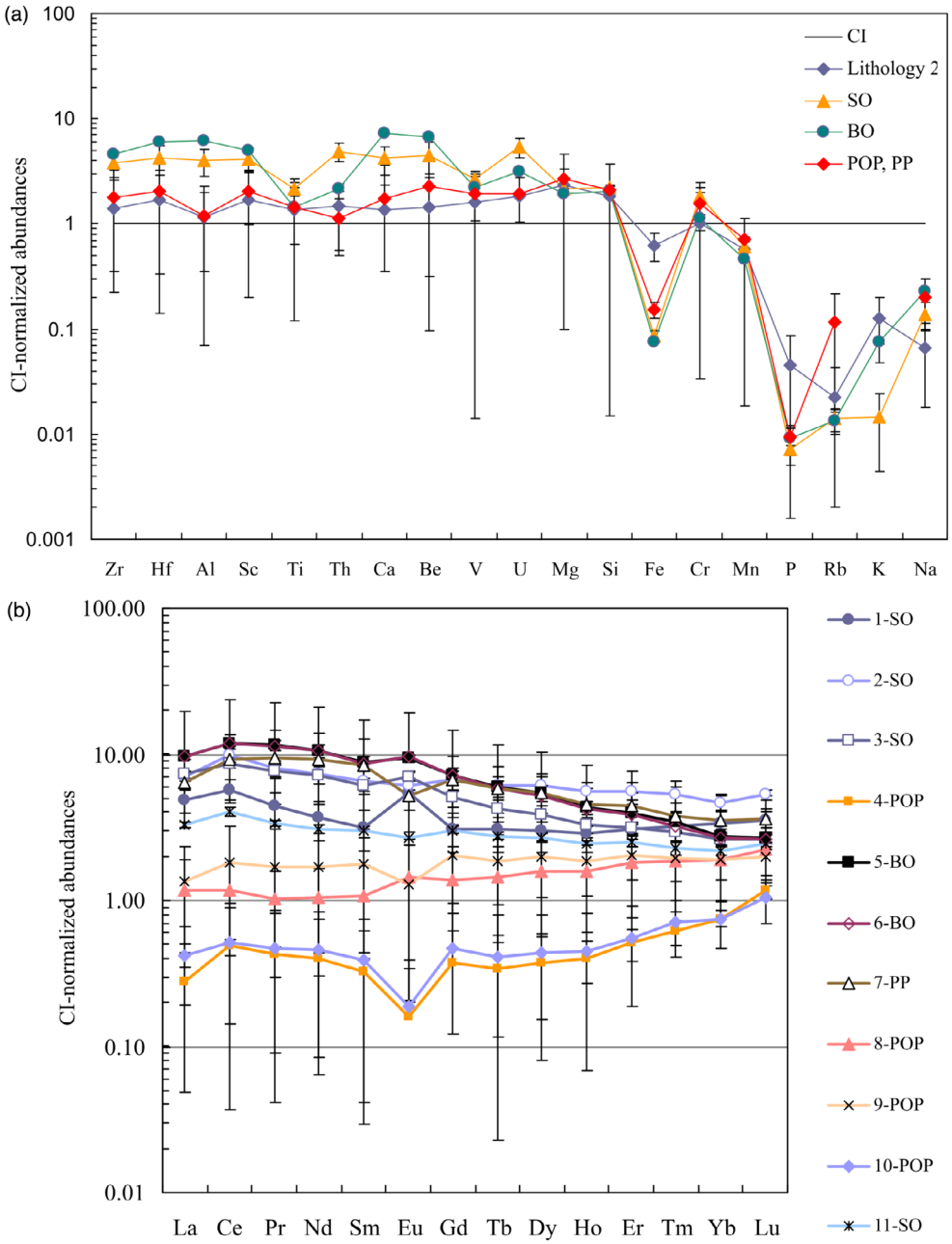

Fig. 9. a) Average chemical composition of SO, BO, POP, and PP chondrules from lithology 1and different silicate areas from lithology 2 of SG 013 normalized to the CI composition (Anders & Grevesse, 1989). b) Average REE abundance of silicate chondrules and clasts from lithology 1. Standard deviations are shown as black bars. (Color figure can be viewed at wileyonlinelibrary.com.)

mentioned above, such as the presence of two lithologies with different metal abundances and porphyritic chondrules, may be attributed to the wide variation of components in the CB parent body as has been shown for Isheyevo (CH/CBb) (Ivanova et al., 2008; Krot et al., 2007). The L1 and L2 lithologies do not contain any CAIs, similar to most CBa chondrites.

Formation of SG 013 Lithologies and Their Components

We recognized that both lithologies of SG 013 may have formed in the CB reservoir based on their mineral chemistry and bulk oxygen composition, which are typical for CBa chondrites (Weisberg et al., 2001). Although the lithologies have different textures—L2 is achondrititc recrystallized and reminiscent of the

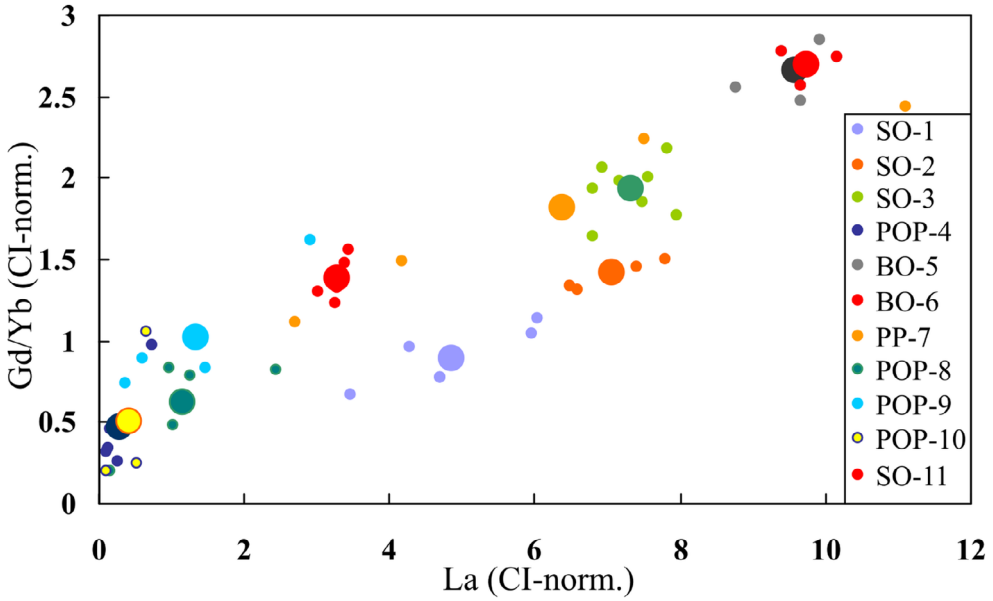

Fig. 10. Gd/Yb versus La normalized to CI. The plot clearly shows a correlation between LREE enrichment and high REE slope in all the SG 013 silicate objects. All data of every chondrule and clasts are shown by different colors similar to the color of the average composition of each silicate object. (Color figure can be viewed at wileyonlinelibrary.com.)

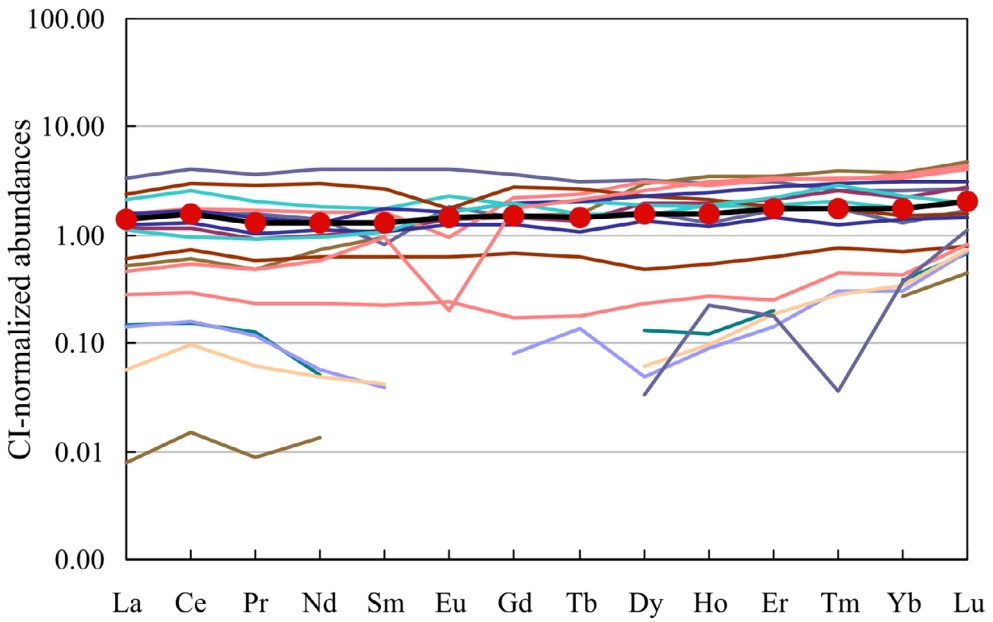

Fig. 11. REE compositions of 18 different silicate areas of lithology 2 of SG 013 and average composition of the silicate portion of L2 normalized to CI composition (Anders & Grevesse, 1989). (Color figure can be viewed at wileyonlinelibrary.com.)

recrystallized matrix of Fountain Hills (Cba)—their formation may be considered based on the main scenario for CBa chondrite origin.

Based on the apparent absence of interchondrule fine-grained matrix material in CB chondrites and their young age, Krot et al. (2005) proposed that the CB plume event occurred after nearly complete dissipation of the accretionary disk, during the debris stage of its evolution (Krot et al., 2021). Subsequently, Meibom et al. (2005) suggested that interchondrule and intermetal shock melts in CB chondrites may represent the remains of the missing matrix. Based on a physical model for the formation of chondrules and chondrites (Stewart et al., 2019a, 2019b), mutual collisions between dynamically

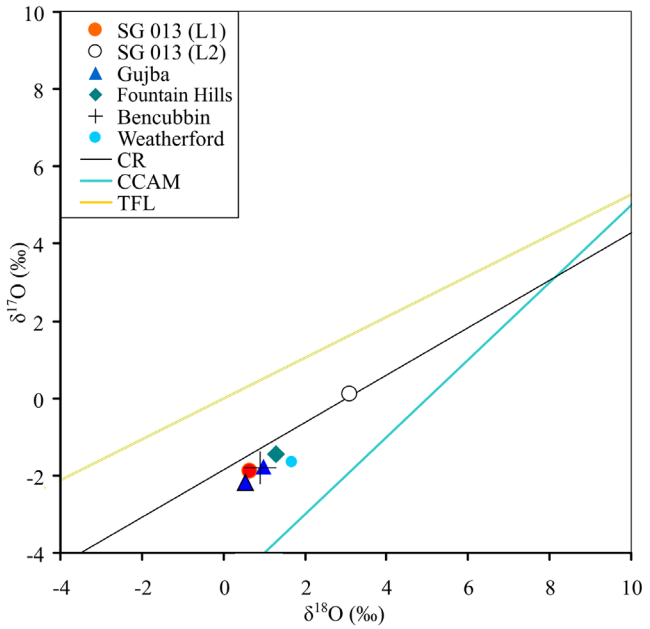

Fig. 12. Bulk oxygen isotopic compositions of SG 013, in two lithologies (L1, L2) compared to those of Gujba, Bencubbin, Weatherford, and Fountain Hills. TFL = terrestrial fractionated line; CCAM = carbonaceous chondrite anhydrous minerals line. CR = CR chondrite trend line. (Color figure can be viewed at wileyonlinelibrary.com.)

coexisting planetesimals produce impact vapor plumes that collapse and concentrate a size-sorted mixture of chondrules and dust. The warm cloud of shock-heated gas, dust, and chondrules is a dynamic and thermal anomaly in the nebula with characteristics that assist with new planetesimal formation. It was suggested that CB plume material accreted together with "normal" chondritic material that predated the plume event and was probably present in the disk. Since CB and CH chondrites are genetically related, the presence of different aqueously altered chondritic lithic clasts, metamorphosed chondrules, heavily metamorphosed clasts, and fragments of an angrite-like asteroid observed in CH chondrites could be consistent with this late stage of disk evolution (Krot et al., 2021). Some of the "normal" chondritic components may have been heated conductively by the silicate vapor of the expanding plume and bow shocks (Stewart et al., 2019a, 2019b).

Sierra Gorda 013 is similar to the Fountain Hills CBa chondrite (Weisberg & Ebel, 2009) in abundances of POP and BO chondrules and low sulfide content. A low abundance of alkalis (Fig. 9a), which is typical for CBa chondrites, may be consistent with SG 013 chondrule formation in a high-temperature region. The formation of porphyritic chondrules requires either solid chondrule precursors which survived during chondrule melt cooling due to lower peak temperature than their liquidus temperature (Lofgren & Russell, 1986), or a large amount of dust to form nucleation sites in the chondrule melt (Connolly & Hewins, 1995). Thus, the presence of porphyritic chondrules in SG 013 suggests that these chondrules formed by (1) incomplete melting of solid precursors or (2) by melt formation in the presence of dust grains. The lack of fine-grained matrix in SG 013 may rule out (2).

Ca-Al-rich SO chondrules are impact plume-produced components of CB chondrites (Krot et al., 2021). It was suggested that SO chondrules crystallized from melts that experienced partial evaporation in the CB plume (Krot et al., 2007), and it seems likely that some nonporphyritic chondrules in CB chondrites could have formed by complete melting of pre-existing chondrules entrained in the plume. Some porphyritic chondrules entrained in the lower temperature peripheral portions of the CB plume could have experienced incomplete melting resulting in the formation of a new generation of porphyritic chondrules (Krot et al., 2021). The fact that chromite is concentrated in the peripheral parts of SO chondrules of SG 013 L1, and olivine bars throughout the chondrule transformed into pyroxene bars with chromite may indicate that olivine experienced incongruent melting and chromite could be a by-product of this melting. This is consistent with very low Cr content in olivine in both lithologies of SG 013 compared to that of Bencubbin and Weatherford (Fig. 6c).

Thus, L1 and L2 of SG 013 could represent a mixture of size-separated fractions of the impact products of a catastrophic collisional event and "normal" chondritic material affected by heating due to silicate vapor and bow shocks under various temperature and redox conditions. They could have formed separately, in different temperatures and local redox environments and later combined together. The small silicate inclusions surrounding the metal globules from L1 may have adhered to the metal globules during or after the collision event.

The absence of sulfides in L2 and their low abundance in L1 of SG 013 could be connected with decomposition of sulfides and evaporation of sulfur in an impact plume under local oxidizing conditions and reaction of sulfur with oxygen. As shown in experimental work (Gooding & Muenow, 1977), above 800 °C metal vapor began to appear in the company of sulfur gases (S_2 and SO_2) and increased in absolute abundance to the termination of measurements at 1300 °C. For SG 013, the local more oxidizing environment in the plume resulted in formation of mostly SO_2 instead of S_2 to avoid recondensation of sulfur back to the material.

Fedkin et al. (2015) and Oulton et al. (2016) suggested that differentiated bodies with Fe,Ni-metal

Table 6. Comparison of two lithologies (L1 and L2) of SG 013 with CBa and CBb chondrites and Fountain Hills.

	Texture	Chondrules	Matrix	CAIs	Metal abundance	Sulfide	Chromite
SG 013, L1	Chondritic, metal globules 0.6 cm chondrules 0.5 cm	POP, BO, and SO	No	No	80 vol%	Rare	Exist
SG 013, L2	Recrystallized, metal and silicate grains, 0.05–0.2 mm	No	No	No	25 vol%	No	Exist
Fountain Hills	Chondritic, metal grains and chondrules, 0.4 cm	POP, BO, and CC	Recrystallized	No	26 vol%	Rare	Spinel
CBa chondrites (Bencubbin, Gujba, Weatherford)	Globules of metal, chondrules, and clasts, ~1 cm	BO and CC	Dark inclusions (matrix lumps)	Rare	>60 vol%	Exist	No
CBb chondrites (Hammadah al Hamra 237, Queen Alexandra Range 94411)	Chondritic, metal grains and chondrules, up to 1 mm	BO, CC, and SO	Matrix lumps fine-grained	Exist 0.4 mm	>70 vol%	Exist	No

Data for Fountain Hills (Lauretta et al., 2004, 2009), CBa and CBb (Krot et al., 2002; Weisberg et al., 2001).

core and silicate mantle and crust were involved in the CB collision event. In this scenario, the precursors of SO chondrules may represent the Ca, Al-rich basaltic crust of these bodies melted and vaporized in different proportions. Fe,Ni-metal grains formed by melting and evaporation of the metal core followed by gas–liquid and gas–solid condensation in different parts of the plume at different total pressure and metal/hydrogen gas enrichment (Krot et al., 2021). To investigate precursors of the colliding material, we analyzed the primary nature of the SG 013 lithologies.

Precursor Materials of the SG 013 Components

The metal in L1 clearly comprises two compositional groups (a) CB-like metal with an ~10× chondritic flat distribution of the highly refractory siderophile elements (HRSE) and moderate refractory elements, and depletion in volatile elements like the CB chondrite metal (Campbell et al., 2002; Krot et al., 2002; Weisberg et al., 1995); and (b) HRSE-depleted and volatile-depleted siderophile elements metal similar to group (a) (Fig. 8). The CB-like metal (a) could be a result of volatile siderophile element evaporation from the metal due to a catastrophic collision of the precursor bodies. Metal (b) is unusual due to its depletion of HRSE and highly volatile elements with a pattern similar to metal (a). Since it is not quite a complementary composition for metal (a), we may suggest that if metal (b) was formed before the SG 013 accretion, it could be formed as a low-temperature condensate depleted in HRSE and mixed with the metal typical for the CB metal (a).

In metal globules of L1, the Pd/Ir ratios drastically vary from 0.44 to 7.49. A strong variation of Pd/Ir ratios could be the result of condensation of metal from a metal-enriched vapor plume at much higher temperatures and pressures than condensation in a canonical solar nebula (Campbell et al., 2002). However, Fedkin et al. (2015) recognized that the compositions of the CBb silicate clasts described by Krot et al. (2001) could not be condensed from a vapor plume formed by collision between a metal impactor and a chondritic target, and the CBb silicate clasts could only fit condensate compositions if the silicate target was differentiated into crust and mantle, and the vapor plume inherited part of the chemical heterogeneity of the target.

The geochemistry of L1 silicate clasts and chondrules shows that the silicate portion of L2 and porphyritic chondrules has similar average composition (Fig. 9a): almost chondritic, pattern, small enrichment of refractory elements, and depletion of moderate volatiles with the exception of Cr and depletion of volatile elements. Enrichment of Cr could be connected with the primary source of material of both lithologies, which were enriched in Cr. Unlike porphyritic

chondrules and clasts and L2 average bulk compositions of silicates, nonporphytitic chondrules (SO and BO) are enriched in refractory elements and depleted in moderate (also with the exception of Cr) and highly volatile elements similar to Ca-Al-rich SO chondrules of CB chondrites described by Krot et al. (2007, 2021) indicating an evaporation process. However, all chondrules and clasts from L1 have very different fractionated bulk REE compositions and they are not similar to the bulk REE composition of L2, which has flat chondritic REE distributions. Differences in composition of some areas of L2 may be explained by different mineral proportions.

All the silicate chondrules of L1 and at least some areas of L2 exhibit a weak positive Ce anomaly (Fig. 9b). Ce/Ce* ratios vary from 1.20 to 1.39, and only one chondrule has Ce/Ce* ratio 1.08. The average Ce enrichments in the lithologies are different: L1 has Ce up to 5.6xCI while the average of L2 lacks a Ce anomaly. The Ce anomaly could be attributed to recondensation from a vapor formed by evaporating silicates under relatively oxidizing conditions (Wang et al., 2001). It could be explained by presumable evaporation of the L1 precursor in variable local redox conditions due to a different gas/dust ratio in the hot plume or by more oxidized composition of one of the colliding bodies. Oulton et al. (2016) noted that an impact plume is a distinctly nonequilibrium process where oxidizing vapor generated at silicate melt interfaces mixes with surrounding hydrogen-bearing nebular gas, creating sharp gradients in oxygen fugacity. Under such conditions, volatile CeO_2 would be reduced to refractory Ce_2O_3, which would rapidly condense into the silicate melt, thereby creating positive Ce anomalies.

It is interesting to note that several clasts from L1 (e.g., BO chondrule #6) have REE patterns similar to that of the BHVO basalt REE distribution (Fig. 13) although the concentrations of REE in BO #6 are five times less than those in BHVO basalt. This supports the possibility that the precursors of these chondrules and clasts may represent the Ca, Al-rich basaltic crust of large bodies melted and vaporized in different proportions (Oulton et al., 2016). The REE distribution pattern of L1 chondrules and clasts (Fig. 9b) has LREE enrichment up to 2-6xCI, while L2 has mostly chondritic distribution and a weak heavy REE (HREE) enrichment that could be explained by the prevalence of olivine and pyroxene in its composition. However, the LREE enrichment or depletion in L1 chondrules and clasts estimated by the La/Sm ratio indicates a high fractionation. This ratio varies in SG 013 objects from 0.9 to 1.8 relative to CI composition. Such variation in the LREE is essentially impossible to accomplish by processes involving vapor–liquid or vapor–solid exchange of REE and appears to have been inherited from a differentiated target (Oulton et al., 2016). It should be noted that igneous processes can create this fractionation because La is more incompatible than Sm. Gd/Yb-La correlations (Fig. 10) in clasts and chondrules of L1 also support this observation. However, none of the REE patterns of chondrules and clasts from SG 013 have similar REE patterns to BO and CC chondrules of the Gujba CBa chondrite (Oulton et al., 2016) with the exception of a similar LREE-depleted pattern of POP chondrule #8, which is similar to chondrule #3-27b from Gujba.

Positive and negative Eu anomalies were observed in the SG 013 L1 chondrules and clasts (Fig. 9b). In reducing gases, Eu is more volatile than other REE, followed by Yb. The Eu/Eu* ratios of L1 chondrules and clasts vary from 0.45 to 1.94, also indicating significant REE fractionation. However, we did not observe Yb anomalies which should form during evaporation/recondensation processes, but do not form during differentiation. Yb/Yb* ratios vary only slightly (0.93–1.02).

The L1 material could preserve the traces of igneous differentiated precursors, while L2 had primitive chondritic precursor material. Due to oxygen isotopic similarity to the CR trend and relative older ages of CR chondrules compared to ages of CB chondrules (Krot et al., 2005), we can propose an igneous CR-like precursor for SG 013. The L1 precursor material could have been modified by igneous processes and then, in the plume, could have been affected by melting and evaporation in different degrees that resulted in the formation of SO and BO chondrules. The material of L2 is similar to POP chondrules of L1 in bulk major and trace chemistry but different in the metal content. Thus, we propose that the L2 material could possibly be a precursor material for POP chondrules of L1 and one of the colliding bodies which took part in the catastrophic event.

Secondary Processes in Formation of SG 013

SG 013 lithology 1 was affected by shock up to S5, which resulted in only local melting areas between the metal globules and chondrules and formation of melt pockets, and the rock is not metamorphosed. The partial melting of the metal due to the shock events resulted in the silicate–metal melt observed between metal globules. However, we did not observe any typical characteristics of secondary impact processing described by Srinivasan et al. (2017) for CBa and CBb chondrites due to the generally low abundance of sulfides in SG 013. The texture of L2 resembles highly metamorphosed chondrites and the recrystallized matrix

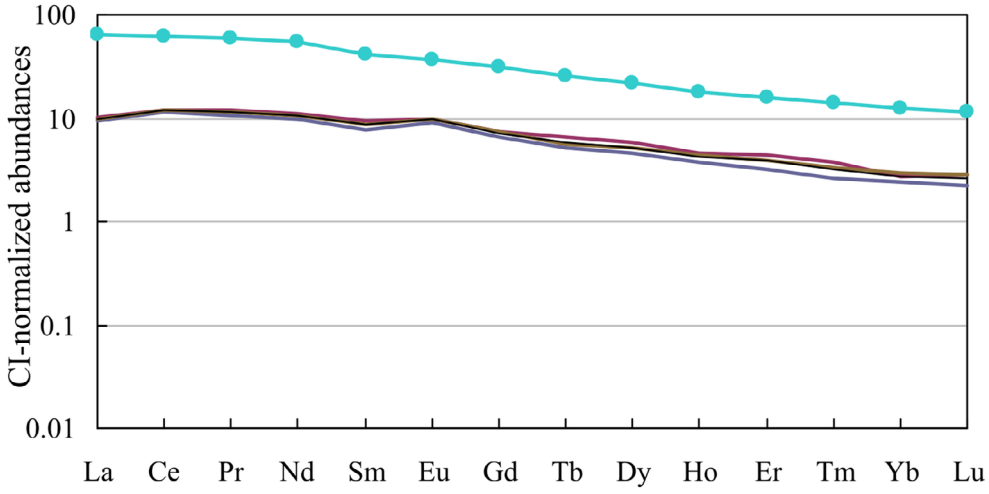

Fig. 13. REE composition of BO chondrule #6 from lithology 1 of SG 013 compared to the Hawaiian basalt, BHVO from Kilauea (blue square). (Color figure can be viewed at wileyonlinelibrary.com.)

of Fountain Hills (Weisberg & Ebel, 2009) corresponds to type 6 recrystallized chondrites, and was affected by thermal metamorphism at 800–900 °C. Thus, the lithologies likely combined relatively late, after the formation of the CBa parent body. Oxygen isotopic composition of L2 could be slightly modified due to metamorphism and shifted along the CR chondrite trend line.

The presence of symplectites in large BO chondrules of SG 013 L1 is not typical for CB and other chondrites; however, similar symplectites were reported in the partially fractionated LL chondritic rock NWA 6485 (Lorenz et al., 2019). Bell et al. (1975) classified the symplectites in lunar rocks in six types (A–F) by morphology, petrographic position in the host rock, and by the host rock petrology. In general, two main types of symplectites are distinguished (Khisina & Lorenz, 2015): Type I are micron-sized lamellae or rosettes settled within the host olivine crystals, oriented according to its crystallographic planes, and composed of submicron grains of chromite and clinopyroxene (e.g., Gooley et al., 1974; Greshake et al., 2000; Khisina et al., 2013; Markl et al., 2001; Mikouchi et al., 2000). Type II are more coarse-grained, microcrystalline intergrowths of chromite and pyroxene (Ca-pyroxene or/low-Ca pyroxene) occurring as pockets in the olivine at the contacts with surrounding phases, pyroxene or feldspar. Symplectites of type II were observed in lunar rocks (Bell et al., 1975), diogenites (Irving et al., 2003; Mittlefehldt, 2000), howardites (Lorenz et al., 2001, 2010, 2014), and HED-related peridotites (Goodrich & Righter, 2000). The symplectites found in SG 013 consist of chromite and low- or high-Ca pyroxene occurring in olivine at the contact with feldspar and are similar to the type II symplectites reported in the partially fractionated LL chondritic rock NWA 6485 (Lorenz et al., 2019).

Several mechanisms have been proposed to explain the origin of symplectites (e.g., review of Holness et al., 2011). The mechanisms of type II symplectite origin include crystallization of trapped late-stage melt (Albee et al., 1975; Bell et al., 1975; Dymek et al., 1975; Gooley et al., 1974), or reaction of Cr diffusing out of olivine (Bell et al., 1975) or from pre-existing chromite (Gooley et al., 1974) and reaction between olivine and plagioclase. The occasional occurrence of symplectites in the olivine crystals of the SG 013 barred chondrules, their association with relatively coarse-grained chromite and pyroxene, seems not to be a result of diffusional segregation of trace elements at any preferred crystallographic plane or grain boundaries of the host olivine. We propose that chondrules enriched in chromite were locally remelted during the shock events. This was local shock melting due to the propagation of a heterogeneous front of shock pressure, so some chromite-bearing areas of chondrules were melted while other areas were not affected by melting and retained unmelted chromite grains. An absence of the incoming chromite-bearing channels or veins and general isolation of the chondrule clasts at their molten stage should exclude the symplectite formation from the reaction of the chondrule with exogenous Cr sources. We propose that, in a case of SG 013, the symplectites' formation mechanism could resemble the mechanism of captured melt crystallization mentioned above during the local shock remelting of chondrule areas composed by olivine, pyroxene, anorthite, and chromite (Fig. 3b). The equilibrium temperature for coexisting low- and high-Ca pyroxenes in symplectites was estimated as

~900 °C (Lindsley, 1983). The fine-grained texture of the chondrule mesostasis probably formed during the relatively slow subsolidus cooling down to this temperature, and after that, the chondrules were quickly cooled.

CONCLUSIONS

SG 013 is an unusual anomalous CBa-like meteorite breccia found as two paired stones. SG 013 contains two texturally and mineralogically different lithologies: L1 has affinity to the CBa subgroup of chondrites containing ~80 vol% of metal, and L2 is recrystallized like a highly metamorphosed chondrite with ~25 vol% of metal. The reduced composition of olivine and pyroxene, anorthitic glass in mesostasis, Ni-Co contents in metal, and bulk oxygen isotopic compositions of L1 correspond to CBa chondrites. However, the presence of porphyritic chondrules along with SO and BO chondrules, a low abundance of sulfides in L1 as well as abundant chromite, silicate, and glassy inclusions in the metal globules distinguish SG 013 L1 from other CBa chondrites. Silicates of L2 are similar to those of CBa chondrites in composition. Metal is represented by low-Ni and high-Ni phases in L1 and L2 unlike CBa chondrites. The L2 oxygen isotopic composition differs somewhat from L1 but belongs to the CR-chondrite oxygen isotopic composition trend.

Siderophile chemistry of metal globules and bulk major and trace element chemistry of SG 013 chondrules and clasts from L1 indicate fractionation during melting and evaporation. The REE distribution of the L1 chondrules records the traces of possible differentiation processes in formation of the L1 precursor. The bulk major and trace element chemistry of the silicate portion of L2 is similar to that of POP chondrules and clasts of L1, although the average REE composition of L2 is chondritic.

SG 013's origin may be explained by collision of planetesimals resulting in a hot plume and subsequent evaporation and condensation of precursor material. We conclude that L1 and L2 were formed from a primitive chondritic precursor and possibly differentiated material, which collided to form SG 013. The silicate portion of L2 may represent a precursor material for the POP chondrules of L1 based on similarity in their bulk composition. SG 013 contains components probably formed in different parts of an impact plume under different conditions, as it has porphyritic clasts and chondrules along with nonporphytitic chondrules, losing alkalis and sulfur.

After accretion, both lithologies were affected by secondary shock events and thermal metamorphism. Shock events led to formation of shock melt areas between metal globules and silicate chondrules and clasts of L1 and to the partial silicate–metal melting. Local partial melting of chondrules resulted in formation of symplectites in L1 chondrules. Thermal shock metamorphism resulted in recrystallization of the material of L2.

Acknowledgments—We thank Sergei E. Borisovsky for his help with some BSE images using JEOL JXA-8200 (IGEM; Institute of Geology of Ore Deposits, Petrography, Mineralogy and Geochemistry of Russian Academy of Sciences, Staromonetny per. 35, Moscow 119017, Russia). We very appreciate Associate Editor, Kevin Righter, and reviewers, Rhian Jones and Sasha Krot, for their fruitful reviews which helped to improve this paper. This work was partially supported by the Russian Fund of Basic Research (RFBR) (grant #20-05-00117) and it was a part of research contribution of the program #0137-2019-0002. Research at the National High Magnetic Field Laboratory is supported by the US National Science Foundation through NSF/DMR-1644779 and the State of Florida, and by NASA Emerging Worlds (#80NSSC18K0595).

Data Availability Statement—Data available on request from the authors.

Editorial Handling—Dr. Kevin Righter

REFERENCES

Agee, C. B., Vaci, Z., Ziegler, K., and Spilde, M. N. 2019. Northwest Africa 12273: Unique Ungrouped Metal-Rich Chondrite (Abstract #1176). 50th Lunar and Planetary Science Conference. CD-ROM.

Albee, A. L., Dymek, R. F. & DePaolo, D. J. 1975. Spinel Symplectites: High Pressure Solid-State Reaction or Late-Stage Magmatic Crystallization? (Abstract). Proceedings, 6th Lunar Science Conference. p. 1.

Amelin, Y. U., and Krot, A. N. 2002. Pb Isotopic Age of Chondrules from the CR Carbonaceous Chondrite Acfer 059. *Meteoritics & Planetary Science* 37(Supplement): A12.

Amelin, Y., and Krot, A. N. 2005. Young Pb-Isotopic Ages of Chondrules in CB Carbonaceous Chondrites (Abstract #1247). 36th Lunar and Planetary Science Conference. CD-ROM.

Anders, E., and Grevesse, N. 1989. Abundances of the Elements: Meteoritic and Solar. *Geochimica et Cosmochimica Acta* 51: 197–214.

Bell, P. M., Mao, H. K., Roedder, E. & Weiblen, P. W. 1975. The Problem of the Origin of Symplectites in Olivine-Bearing Lunar Rocks. Proceedings, 6th Lunar Science Conference. pp. 231–48.

Bollard, J., Connelly, J., and Bizzarro, M. 2015. Pb-Pb Dating of Individual Chondrules from the CBa Chondrite Gujba: Assessment of the Impact Plume Formation Model. *Meteoritics & Planetary Science* 50: 1197–216.

Bouvier, A., Gattacceca, J., Agee, C., Grossman, J., and Metzler, K. 2017. The Meteoritical Bulletin No. 104. *Meteoritics & Planetary Science* 1: 247.

Campbell, A. J., Humayun, M., Meibom, A., Krot, A. N., and Keil, K. 2001. Origin of Zoned Metal Grains in the QUE 94411 Chondrite. *Geochimica et Cosmochimica Acta* 65: 163–80.

Campbell, A. J., Humayun, M., and Weisberg, M. K. 2002. Siderophile Element Constraints on the Formation of Metal in the Metal-Rich Chondrites Bencubbin, Gujba and Weatherford. *Geochimica et Cosmochimica Acta* 66: 647–60.

Campbell, A. J., Humayun, M., and Weisberg, M. K. 2005. Compositions of Unzoned and Zoned Metal in the CBb Chondrites Hammadah al Hamra 237 and Queen Alexandra Range 94627. *Meteoritics & Planetary Science* 40: 1131–48.

Clayton, R. N., and Mayeda, T. K. 1999. Oxygen Isotope Studies of Carbonaceous Chondrites. *Geochimica et Cosmochimica Acta* 63: 2089–104.

Connelly, J. N., Bizzarro, M., Krot, A. N., Nordlunds, A., Wielandt, D., and Ivanova, M. A. 2012. The Absolute Chronology and Thermal Processing of Solids in the Solar Protoplanetary Disk. *Science* 338: 651–5.

Connolly, H. C., and Hewins, R. H. 1995. Chondrules as Products of Dust Collisions with Totally Molten Droplets Within a Dust-Rich Nebular Environment—An Experimental Investigation. *Geochimica et Cosmochimica Acta* 59: 3231–46.

Dymek, R. F., Albee, A. L. & Chodos, A. A. 1975. Comparative Petrology of Lunar Cumulate Rocks of Possible Primary Origin: Dunite 72415, Troctolite 76535, Norite 78235, and Anorthosite 62237. Proceedings, 6th Lunar Science Conference. pp. 301–41.

Fedkin, A. V., Grossman, L., Humayun, M., Simon, S. B., and Campbell, A. J. 2015. Condensates from Vapor Made by Impacts Between Metal-, Silicate-Rich Bodies: Comparison with Metal and Chondrules in CB Chondrites. *Geochimica et Cosmochimica Acta* 164: 236–61.

Gattacceca, J., McCubbin, F. M., Bouvier, A., and Grossman, J. N. 2020. The Meteoritical Bulletin, No. 108. *Meteoritics & Planetary Science* 55: 1146–50.

Gooding, J. L., and Muenow, D. W. 1977. Experimental Vaporization of the Holbrook Chondrite. *Meteoritics* 12: 401–8.

Goodrich, C. A., and Righter, K. 2000. Petrology of Unique Achondrite Queen Alexandra Range 93148: A Piece of the Pallasite (Howardite-Eucrite-Diogenite?) Parent Body? *Meteoritics & Planetary Science* 35: 521–36.

Gooley, R., Brett, R., Warner, J., and Smyth, J. R. 1974. A Lunar Rock of Deep Crustal Origin: Sample 76535. *Geochimica et Cosmochimica Acta* 38: 1329–39.

Greenwood, R. C., Burbine, T. H., Miller, M. F., and Franchi, I. A. 2016. Melting and Differentiation of Early-Formed Asteroids: The Perspective from High Precision Oxygen Isotope Studies. *Chemie der Erde—Geochemistry* 7: 1–43.

Greshake, A., Stephen, T., and Rost, D. 2000. Combined TEM and TOF_SIMS Study of Symplectic Exsolutions in Olivine from Martian Meteorites Nakhla and Governador Valadarez (Abstract #1150). 31st Lunar and Planetary Science Conference. CD-ROM.

Holness, M. B., Stripp, G., Humphreys, M. C. S., Veksler, I. V., Nielsen, T. F. D., and Tegner, C. 2011. Silicate Liquid Immiscibility Within the Crystal Mush: Late-Stage Magmatic Micro-Structures in the Skaergaard Intrusion, East Greenland. *Journal of Petrology* 52: 175–222.

Humayun, M. 2012. Chondrule Cooling Rates Inferred from Diffusive Profiles in Metal Lumps the Acfer 097 CR2 Chondrite. *Meteoritics & Planetary Science* 47: 1191–208.

Humayun, M., Davis, F. A., and Hirschmann, M. M. 2010. Major Element Analysis of Natural Silicates by Laser Ablation ICP-MS. *Journal of Analytical Atomic Spectrometry* 25: 998–1005.

Irving, A. J., Kuehner, S. M., Rumble, D. III, Hupe, A. C., and Hupe, G. M. 2003. Olivine Diogenite NWA 1459: Plumbing the Depths of 4 Vesta (Abstract #1502). 34th Lunar and Planetary Science Conference. CD-ROM.

Ivanova, M. A., Kononkova, N. N., Krot, A. N., Greenwood, R. C., Franchi, I. A., Verchovsky, A. B., Trieloff, M., Korochansteva, E. V., and Brandstaetter, F. 2008. The Isheyevo Meteorite: Mineralogy, Petrology, Bulk Chemistry, Oxygen, Nitrogen, Carbon Isotopic Compositions and ^{40}Ar-^{39}Ar Ages. *Meteoritics & Planetary Science* 43: 915–40.

Ivanova, M. A., Ma, C., Lorenz, C. A., Franchi, I. A., and Kononkova, N. N. 2019. A New Unusual Bencubbinite (CBa), Sierra Gorda 013, and its Unique V-Rich Sulfides. *Meteoritics & Planetary Science* 54: A.185.

Jansen, C. A., Brenker, F. E., Krot, A. N., Zipfel, J., Pack, A., Labenne, L., Bizzarro, M., and Schiller, M. 2019. Mineralogy, Petrology, and Oxygen Isotopic Composition of Northwest Africa (NWA) 12379, a New Metal-Rich Chondrite with Affinity to Ordinary Chondrites. *Geochemistry* 79: 125537.

Kallemeyn, G. W., Boynton, W. V., Willis, J., and Wasson, J. T. 1978. Formation of Bencubbin Polymict Meteoritic Breccia. *Geochimica et Cosmochimica Acta* 42: 507–15.

Khisina, N. R., and Lorenz, C. A. 2015. Dehydrogenation as the Mechanism of Formation of the Oriented Spinel-Pyroxene Symplectites and Magnetite-Hematite Inclusions in Terrestrial and Extraterrestrial Olivines. *Petrology* 23: 176–88.

Khisina, N. R., Wirth, R., Abart, R., Rhede, D., and Heinrich, W. 2013. Oriented Chromite-Diopside Symplectic Inclusions in Olivine from Lunar Regolith Delivered by "Luna-24" Mission. *Geochimica et Cosmochimica Acta* 104: 84–98.

Koch, T. E., Brenker, F. E., Krot, A. N., and Bizzarro, M. 2016. Petrography of Quebrada Chimborazo 001—A New CBa Chondrite (Abstract #1968). 47th Lunar and Planetary Science Conference. CD-ROM.

Koch, T. E., Brenker, F. E., Prior, D. J., Jilly, K., Krot, A. N., and Bizarro, M. 2019. Shock History of the Metal-Rich CB Chondrite Quebrada Chimborazo (QC) 001 (Abstract #6179). 82nd Annual Meeting of the Meteoritical Society.

Krot, A. N., Amelin, Y., Cassen, P., and Meibom, A. 2005. Young Chondrules in CB Chondrites from a Giant Impact in the Early Solar System. *Nature* 436: 989–92.

Krot, A. N., Ivanova, M. A., and Ulyanov, A. A. 2007. Chondrules in the CB/CH-Like Carbonaceous Chondrite Isheyevo: Evidence for Various Chondrule-Forming Mechanisms Multiple Chondrule Generations. *Chemie der Erde* 67: 283–300.

Krot, A. N., Keil, K., Goodrich, C., Weisberg, M. K., and Scott, E. R. D. 2014. Classification of Meteorites. In *Meteorites and Cosmochemical Processes*, edited by A. M. Davis, 1−63. Vol. 1 Treatise on Geochemistry, 2nd Ed.

(Exec. Eds. H. D. Holland and K. K. Turekian). Oxford: Elsevier.

Krot, A. N., Meibom, A., Russell, S. S., Alexander, C. M. O'D., Jeffries, T. E., and Keil, K. 2001. A New Astrophysical Setting for Chondrule Formation. *Science* 291: 1776–9.

Krot, A. N., Meibom, A., Weisberg, M. K., and Keil, K. 2002. The CR Chondrite Clan: Implications for Early Solar System Processes. *Meteoritics & Planetary Science* 37: 1451–90.

Krot, A. N., Nagashima, K., Bizzarro, M., Huss, G. R., Davis, A. M., McKeegan, K. D., Meyer, B. S., and Ulyanov, A. A. 2008. Multiple Generations of Refractory Inclusions in the Metal Rich Carbonaceous Chondrites Acfer 182/214 and Isheyevo. *The Astrophysical Journal* 672: 713–21.

Krot, A. N., Nagashima, K., Libourel, G., and Miller, K. E. 2018. Multiple Mechanisms of Transient Heating Events in the Protoplanetary Disk: Evidence from Precursors of Chondrules and Igneous Ca, Al-Rich Inclusions. In *Chondrules: Records of the Protoplanetary Disk Processes*, edited by S. S. Russel, H. C. Connolly Jr., and A. N. Krot, 11–57. Cambridge, UK: Cambridge University Press.

Krot, A. N., Nagashima, K., and Petaev, M. I. 2012. Isotopically Uniform, ^{16}O-Depleted Calcium, Aluminum-Rich Inclusions in CH and CB Carbonaceous Chondrites. *Geochimica et Cosmochimica Acta* 83: 159–78.

Krot, A. N., Nagashima, K., van Kooten, E. M. M., and Bizzarro, M. 2017. High-Temperature Rims Around Calcium-Aluminum-Rich Inclusions from the CR, CB and CH Carbonaceous Chondrites. *Geochimica et Cosmochimica Acta* 201: 155–84.

Krot, A. N., Nagashima, K., Yoshitake, M., and Yurimoto, H. 2010. Oxygen Isotope Compositions of Chondrules from the Metal-Rich Chondrites Isheyevo (CH/CB$_b$), MAC 02675 (CB$_b$) and QUE 94627 (CB$_b$). *Geochimica et Cosmochimica Acta* 74: 2190–211.

Krot, A. N., Petaev, M. I., Nagashima, K., Dobrică, E., Johnson, B. C., Cashion, M. D., and Rubin, A. 2021. Impact Plume-Formed and Protoplanetary Disk High-Temperature Components in CB and CH Metal-Rich Carbonaceous Chondrites. *Meteoritics & Planetary Science* 56: 1–29.

Lauretta, D. S., Goreva, J. S., Hill, D. H., Killgore, M., La Blue, A. R., Campbell, A., Greenwood, R. C., Franchi, I. A., and Verchovsky, A. B. 2009. The Fountain Hills Unique CB Chondrite: Insights into Thermal Processes on the CB Parent Body. *Meteoritics & Planetary Science* 44: 823–38.

Lauretta, D. S., Killgore, M., Greenwood, R. C., Verchovsky, A. B., and Franchi, I. A. 2004. The Fountain Hills Meteorite: A New CB Chondrite from Arizona (Abstract #1255). 35th Lunar and Planetary Science Conference. CD-ROM.

Lindsley, D. H. 1983. Pyroxene Thermometry. *American Mineralogist* 68: 477–93.

Lofgren, G., and Russell, W. J. 1986. Dynamic Crystallization of Chondrule Melts of and Radial Pyroxene Composition. *Geochimica et Cosmochimica Acta* 50: 1715–26.

Lorenz, C. A., Khisina, N. R., Habler, G., Abart, R., Ntaflos, T. H., and Brandstaetter, F. 2014. Composition of a Pyroxenitic Fragment from the Yurtuk Howardite (Abstract #1777). 45th Lunar and Planetary Science Conference. CD-ROM.

Lorenz, C. A., Kononkova, N. N., and Franchi, I. A. 2019. NWA 6485: Partially Fractionated Chondrite Melt Rock (Abstract #1632). 50th Lunar and Planetary Science Conference. CD-ROM.

Lorenz, C. A., Nazarov, M. A., Brandstaetter, F., and Ntaflos, T. 2010. Metasomatic Alterations of Olivine Inclusions in the Budulan Mesosiderite. *Petrology* 18: 461–70.

Lorenz, C. A., Nazarov, M. A., Kurat, G., Brandstätter, F. & Ntaflos, T. 2001. Clast Population and Chemical Bulk Composition of the Dhofar 018 Howardite (Abstract #1778). 32nd Lunar and Planetary Science Conference. CD-ROM.

Ma, C., and Rossman, G. 2008. Discovery of Tazheranite (Cubic Zirconia) in the Allende Meteorite. *Geochimica et Cosmochimica Acta* 72: A577.

Markl, G., Marks, M., and Wirth, R. 2001. The Influence of T, $a\mathrm{SiO_2}$, and $f\mathrm{O_2}$ on Exsolution Textures in Fe-Mg Olivine: An Example from Augite Syenites of the Ilimaussaq Intrusion, South Greenland. *American Mineralogist* 86: 36–46.

Meibom, A., Petaev, M. I., Krot, A. N., Wood, J. A., and Keil, K. 1999. Primitive Fe,Ni Metal Grains in CH Carbonaceous Chondrites Formed by Condensation from a Gas of Solar Composition. *Journal of Geophysical Research* 104: 22053–9.

Meibom, A., Righter, K., Chabot, N., Dehn, G., Antignano, A., McCoy, T. J., Krot, A. N., Zolensky, M. E., Petaev, M. I., and Keil, K. 2005. Shock Melts in QUE 94411, Hammadah al Hamra 237, and Bencubbin: Remains of the Missing Matrix? *Meteoritics & Planetary Science* 40: 1377–91.

Mikouchi, T., Yamada, I., and Miyamoto, M. 2000. Symplectic Exsolution in Olivine from the Nakhla Martian Meteorite. *Meteoritics & Planetary Science* 35: 937–42.

Miller, M. F., Franchi, I. A., and Pillinger, C. T. 1999. High Precision Measurements of the Oxygen Isotope Mass-Depended Fractionation Line for the Earth-Moon System (Abstract #1729). 30th Lunar and Planetary Science Conference. CD-ROM.

Mittlefehldt, D. W. 2000. Petrology and Geochemistry of the Elephant Moraine Diogenite: A Genomict Breccia Containing a Magnesian Harzburgite Component. *Meteoritics & Planetary Science* 35: 901–12.

Newsom, H. E., and Drake, M. J. 1979. The Origin of Metal Clasts in the Bencubbin Meteorite Breccia. *Geochimica et Cosmochimica Acta* 43: 689–707.

Olsen, M. B., Schiller, M., Krot, A. N., and Bizzarro, M. 2013. Magnesium Isotope Evidence for Single Stage Formation of CB Chondrules by Colliding Planetesimals. *The Astrophysical Journal* 776: L1.

Oulton, J., Humayun, M., Fedkin, A., and Grossman, L. 2016. Chemical Evidence for Differentiation, Evaporation and Recondensation from Silicate Clasts in Gujba. *Geochimica et Cosmochimica Acta* 177: 254–74.

Rubin, A. E., Kallemeyn, G. W., Wasson, J. T., Clayton, R. N., Mayeda, T. K., Grady, M., Verchovsky, A. B., Eugster, O., and Lorenzetti, S. 2003. Formation of Metal and Silicate Globules in Gujba: A New Bencubbin-Like Meteorite Fall. *Geochimica et Cosmochimica Acta* 67: 3283–98.

Rubin, A. E., Ulff-Møller, F., Wasson, J. T., and Carlson, W. D. 2001. The Portales Valley Meteorite Breccia: Evidence for Impact-Induced Melting and Metamorphism of an Ordinary Chondrite. *Geochimica et Cosmochimica Acta* 65: 323–42.

Schrader, D. L., Franchi, I. A., Connolly, H. C., Greenwood, R. C., Lauretta, D. S., and Gibson, J. M. 2011. The Formation and Alteration of the Renazzo-Like Carbonaceous Chondrites I: Implications of Bulk-Oxygen Isotopic Composition. *Geochimica et Cosmochimica Acta* 75: 308–25.

Srinivasan, P., Jones, R. N., and Brearley, A. J. 2017. Compositions and Microstructures of CB Sulfides: Implications for the Thermal History of the CB Chondrite Parent Body. *Meteoritics & Planetary Science* 52: 2193–219.

Stewart, S. T., Carter, P. J., Davies, E. J., Lock, S. J., Kraus, R. G., Root, S., Petaev, M. I., and Jacobsen, S. B. 2019a. Impact Vapor Plume Expansion and Hydrodynamic Collapse in the Solar Nebula (Abstract #1250). 50th Lunar and Planetary Science Conference. CD-ROM.

Stewart, S. T., Carter, P. J., Davies, E. J., Lock, S. J., Kraus, R. G., Root, S., Petaev, M. I., and Jacobsen, S. B. 2019b. Collapsing Impact Vapor Plume Model for Chondrule and Chondrite Formation (Abstract #1251). 50th Lunar and Planetary Science Conference. CD-ROM.

Stoffler, D., Keil, K., and Scott, E. R. D. 1991. Shock Metamorphism of Ordinary Chondrites. *Geochimica et Cosmochimica Acta* 55: 3845–67.

Wang, J., Davis, A. M., Clayton, R. N., Mayeda, T. K., and Hashimoto, A. 2001. Chemical and Isotopic Fractionation During the Evaporation of the FeO-MgO-SiO_2-CaO-Al_2O_3-TiO_2 Rare Earth Element Melt System. *Geochimica et Cosmochimica Acta* 65: 479–94.

Wasson, J. T., and Kallemeyn, G. W. 1990. Allan Hills 85085: A Subchondritic Meteorite of Mixed Nebular and Regolithic Heritage. *Earth and Planetary Science Letters* 101: 148–61.

Weisberg, M. K., and Ebel, D. S. 2009. The Fountain Hills Impact-Modified CB Chondrite Thermal History of the CB Asteroid. *Meteoritics & Planetary Science* 44: 201–10.

Weisberg, M. K., Prinz, M., Clayton, R. N., Mayeda, T. K., Grady, M. M., and Pillinger, C. T. 1995. The CR Chondrite Clan. *Proceedings of the NIPR Symposium on Antarctic Meteorites* 8: 11–32.

Weisberg, M. K., Prinz, M., Clayton, R. N., Mayeda, T. K., Sugiura, N., Zashu, S., and Ebihara, M. 2001. A New Metal-Rich Chondrite Grouplet. *Meteoritics & Planetary Science* 36: 401–18.

Weisberg, M. K., Prinz, M., and Nehru, C. E. 1990. The Bencubbin Chondrite Breccia and its Relationship to CR Chondrites and the ALH85085 Chondrite. *Meteoritics* 25: 269–79.

Yang, S., Humayun, M., and Salters, V. J. M. 2020. Elemental Constraints on the Amount of Recycled Crust in the Generation of Mid-Oceanic Ridge Basalts (MORBs). *Science Advances* 6: eaba2923.

SUPPORTING INFORMATION

Additional supporting information may be found in the online version of this article.

Fig. S1. Data points of LA-ICP-MS investigations of (a) metal of lithology 1; (b) chondrules and clasts of lithology 1 of SG 013; (c) silicate areas of lithology 2.

Fig. S2. X-ray mapping in Kα of Mg (red), Ca (green), Al (blue), and Cr (yellow) of chondrules and clasts from lithology 1 of SG 013. Bright red—olivine, red—pyroxene, blue—mesostasis, yellow—chromite, green—carbonate veins filled by products of weathering. (a) 1-SO, (b) 2-SO, (c) 3-SO, (d) 4-POP, (e) 5-BO, (f) 6-BO, (g) 7-PP, (h) 8-POP, (i) 9-POP, (k) 10-POP, (l) 11-SO.

Fig S3. X-ray maps in Kα of Mg—red, Ca—green, Al—blue of three different areas of lithology 2 from Sierra Gorda 013 chondrite. Yellow—chromite, bright red—olivine, dark red—pyroxene, blue—anorthite, green—terrestrial weathering products; metal is black.